https://doi.org/10.1016/j.compstruct.2021.114892

Curved inserts in auxetic honeycomb for property enhancement and design flexibility

Yu Chen[1,2,3,4], Ming-Hui Fu[5,*], Hong Hu[6,*], Jian Xiong[7]

[1]Packaging Engineering Institute, College of Packaging Engineering, Jinan University, Zhuhai 519070, China

[2]MOE Key Laboratory of Disaster Forecast and Control in Engineering, School of Mechanics and Construction Engineering, Jinan University, Guangzhou 510632, China

[3]Key Laboratory of Product Packaging and Logistics of Guangdong Higher Education Institutes, Jinan University, Zhuhai 519070, China

[4]Zhuhai Key Laboratory of Product Packaging and Logistics, Jinan University, Zhuhai 519070, China

[5]Department of Applied Mechanics and Engineering, Sun Yat-sen University, Guangzhou 510275, China

[6]Institute of Textile and Clothing, The Hong Kong Polytechnic University, Hung Hom, Kowloon, Hong Kong, China

[7]Center for Composite Materials and Structures, Harbin Institute of Technology, Harbin 150001, PR China

E-mail Address: Yu Chen (chenyu362@jnu.edu.cn, chenyu_9101@163.com);

Ming-Hui Fu (stsfmh@mail.sysu.edu.cn, chuanchi_sysu@163.com);

Hong Hu (hu.hong@polyu.edu.hk) ; Jian Xiong (jx@hit.edu.cn)

*Corresponding author: Ming-Hui Fu and Hong Hu

Abstract Imperfect situation, like the non-uniform cross-section or non-straight profile of cell walls, can in certain case be a positive contributor for properties of cellular solids. However, auxetic cellular structures with imperfect profiles for properties enhancement are rarely reported in the literature. Based on the most

common auxetic honeycomb (the re-entrant hexagonal honeycomb, RHH), this paper developed two new types of honeycombs with curved inserts and focused on how microscopic curved inserts in an auxetic honeycomb influence its macroscopic mechanical properties. Theoretical models for the in-plane linear elastic properties of the two types of new honeycombs, including the Young's modulus, Poisson's ratio and shear modulus, were first established, and then verified by numerical simulations. The results showed that the two types of new honeycombs possess the same ability to achieve auxeticity, in the meantime, exhibit improved Young's modulus and shear modulus compared to the RHH. Furthermore, the new honeycombs demonstrate more flexibility in design as the curved inserts can offer more geometric parameters for tailoring their macroscopic mechanical properties. The study also showed that the curved inserts played a key role in determining the dominated deformation mode of the new honeycombs, and a special dominated deformation mode intermediate between pure bending and stretching was found in these honeycombs. The work would provide a useful guide for the development and optimization of auxetic materials.

Keywords: Auxetic; Re-entrant Hexagonal Honeycomb (RHH); Curved Inserts; Elastic Modulus; Theoretical Model

1. Introduction

Cellular structures, including the periodically distributed honeycombs and randomly structured foams, have received considerable attention due to their high specific stiffness and strength [1, 2]. The deformation behavior and mechanical properties of cellular structures depend on their micro-arrangements or topologies. This observation underlies the commonly used concept of mechanical meta-materials, that is, rationally tailoring the micro-arrangements of materials rather than their chemical composition, and some improved, unique or even unexpected properties can be achieved [3], example being the negative Poisson's ratio (NPR). The re-entrant hexagonal honeycomb (RHH) is the most typical case in this regard. Inspired by

nature, the regular hexagonal honeycomb came into people's vision and it has been fully studied over the past decades [1, 4-8]. Interestingly enough, Gibson and Ashby [1] realized that the hexagonal honeycomb in a re-entrant form exhibits an NPR. Five years after Gibson et al.'s finding, in 1987, Lakes [9] successfully fabricated a novel type of NPR polymer foam, which revealed that the NPR materials can be attained in a manmade way. A terminology of "auxetics", that is commonly used today, was introduced by Evans et al. [10] to name these materials. Since then, a consistent trend in the development and characterization of auxetic materials and structures has emerged [11-13].

The main attractiveness of the auxetic materials lies in the negative value of Poisson's ratio (ν) endowing such materials with many improved properties. A simple and well known benefit of introducing such materials is enhancement of their shear modulus given by the common relation in an isotropic body: $G=E/(2+2\nu)$ (G and E respectively denotes the shear and Young's modulus). Apparently, the shear modulus (G) will become infinitely large when ν approaches -1 [14]. Other properties to show an enhanced tendency as ν being negative include the indentation resistance and fracture toughness [15]. In addition, the energy absorption ability of the auxetics is also enhanced. As described by Zhang et al. [16], the re-entrant honeycomb displays higher plateau stress than the regular one and thus finding a better energy absorption performance. It was also reported that the auxetic materials exhibit better shape-fitting ability due to the formation of synclastic curvature under out-of-plane bending [11]. This physical effect of a negative ν can be exploited for some special surfaces, for example, a dome one. Owing to these superior properties mentioned above, the auxetic materials were implemented to a vast number of applications, such as, vibration dampers [17], piezoelectric sensors [18], piezoelectric energy harvester [19], construction materials [20], sports safety equipment [21] and many others.

As the most common auxetic structure, the RHH has been the focus of research for a long time. People have paid a lot of efforts into the modifications on it to achieve

more superior mechanical performance. Bezazi et al. [22] proposed a new centresymmetric cell with edge corners. It was showed that the new configuration allows more degrees of freedom to the designer. Meena and Singamneni [23] conceived a novel S-structures with less stress concentration and more robust auxeticity in comparison with the RHH. Qi et al. [24] replaced the sloped cell wall of the RHH with double circular arc cell walls, which can dissipate extra energy due to more formed plastic angles during the crushing process. Embedding architectures into the RHH has been proved to be an effective way for enhancing the stiffness and strength [25-28]. Rayneau-Kirkhope [29] substituted the solid cell wall of the RHH with sub-structures and obtained a new stiffer auxetic structure. The enhancement mechanism in the embedded enhanced structures [25-28] and the hierarchical configuration [29] is that the micro layout can change the dominated deformation mode of the microstructures from bending to stretching [26, 27]. It has been shown in the literature [30, 31] that the stretching-dominated design is an effective way for the development of stiffer and stronger auxetic structures. Furthermore, the RHH was also extended towards three dimensions by the orthogonal splicing method [32, 33] and the hierarchical design [34].

Obviously, all the mentioned enhanced design schemes acted by tailoring the micro solid distribution or arrangement as the mechanical properties of cellular solids rely on their cell morphology. In practice, the manufacturing process significantly influences the cell morphology of cellular solids and some microstructural imperfections including the non-uniform cross-section of cell walls and non-straight profile of cell walls do exist in real cellular solids [32, 35]. Studies have been delivered to evaluating the effects of microstructural imperfections on the mechanical properties of conventional cellular structures over the past years [36-42]. The results revealed that the imperfections can in certain case be a positive contributor to the structures' stiffness, strength and energy absorption capacity. Furthermore, the imperfections can also provide more tunable geometric parameters, which increase the design flexibility of structures. However, few imperfect situations (non-uniform cross-section of cell walls or non-straight profile of cell walls) were involved in the

auxetic cellular structures.

In this paper, we conceived two novel types of honeycombs developed by endowing the most typical auxetic honeycomb (the RHH) with curved inserts. The two new layouts can be identified as an imperfect case of non-straight profile of cell walls. The focus of this paper lies in a curious issue: how do microscopic curved inserts in an auxetic honeycomb influence its macroscopic mechanical properties? Theoretical models were proposed to predict the in-plane elastic modulus of the newly developed configurations, including the Young's modulus, Poisson's ratio and shear modulus. Finite element (FE) simulations were provided to verify the theoretical results. A systematic comparison between the RHH and the new honeycombs was conducted and fully exploring the effects of the curved inserts on the in-plane mechanical properties of the new honeycombs.

2. RHH with curved inserts

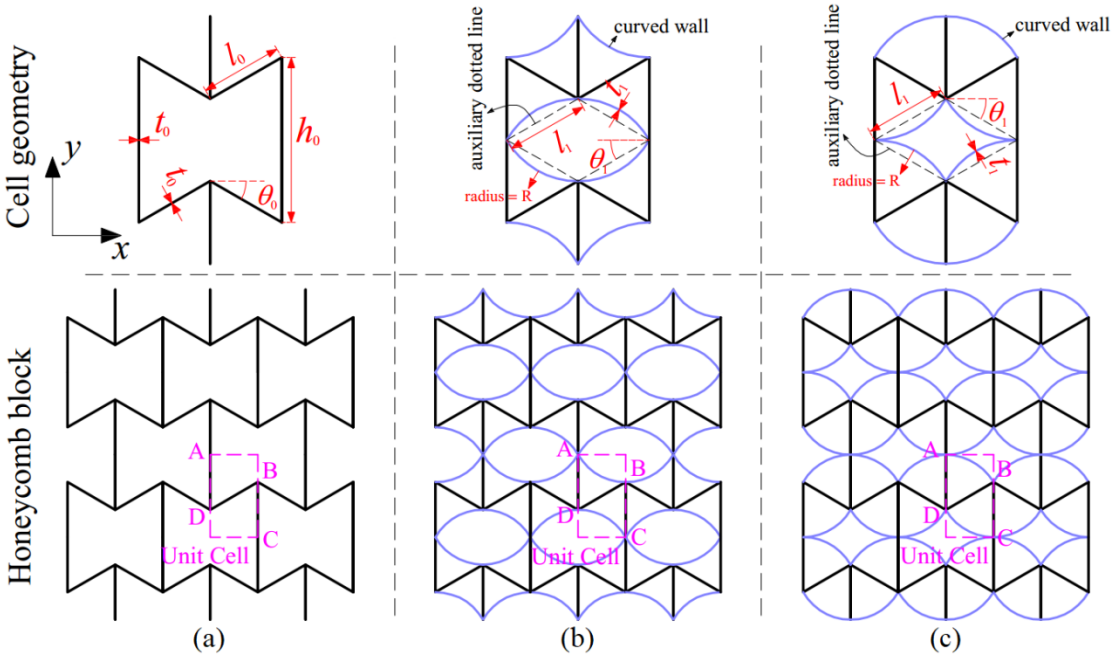

Fig.1. Schematic diagram of the honeycombs: (a) re-entrant hexagonal honeycomb (RHH); (b) RHH with curved insert (Type I new honeycomb); (c) RHH with curved insert (Type II new honeycomb).

Fig.1 displays the re-entrant hexagonal honeycomb (RHH) and the two newly

developed honeycombs. For well depicting the micro-topologies of the two new honeycombs, we constructed four auxiliary lines in the re-entrant hexagonal cell, i.e., the dotted rhombus located in the re-entrant cell, as illustrated in Fig.1(b) and (c). Taking each auxiliary dotted line as a chord, we built an arc with a given radius, R on each side of the respective auxiliary line, and thus forming two kinds of curved quadrangles in the re-entrant cell. Finally, two kinds of new honeycombs were successfully conceived by respectively embedding the two curved quadrangles into every cell of the RHH.

As shown in Fig.1(a), there are four geometric parameters for characterizing the RHH: cell wall thickness (t_0), length of slant wall (l_0), length of vertical wall (h_0) and slant angle (θ_0). Along with the parameters in the basic RHH, the new honeycombs contains two other key geometric parameters: the thickness and the radius of curved wall (t_1 and R). Actually, two auxiliary geometric parameters, the length and the slant angle of the auxiliary line (l_1 and θ_1) are significant for characterizing the new honeycombs. Structurally, l_1 and θ_1 can be written as a function of the given parameters of the RHH:

$$\begin{aligned} l_1 &= l_0\sqrt{\left[\left(h_0/l_0\right)/2-\sin\theta_0\right]^2+\cos^2\theta_0}, \\ \theta_1 &= \arctan\left[\frac{\left(h_0/l_0\right)/2-\sin\theta_0}{\cos\theta_0}\right]. \end{aligned} \tag{1}$$

3. Linear elastic modulus

3.1. Theoretical models

3.1.1. Young's modulus and Poisson's ratio

According to the symmetry of the new honeycombs, a unit cell was determined for analysis, as outlined in Fig.1 (b) and (c). The analytical model of the new honeycomb in Type I is illustrated in Fig.2(a). Four key points (A, B, C and D) are contained in a unit cell we used. Assuming the unit cell undergoes a uniaxial *x*- or *y*-directional stress, The displacements of those key points are listed as follows: vertical

displacement of points A, B and D (v_A, v_B and v_D); horizontal displacement of point B and C (u_B and u_C). It should be noted that the horizontal displacement of points A and D, as well as the vertical displacement of the point C, is equal to zero in our analytical model.

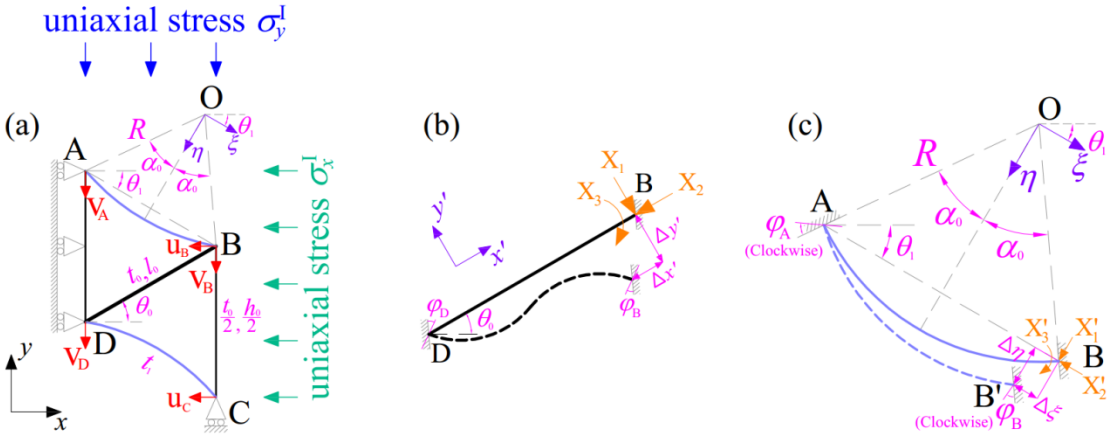

Fig.2. (a) Schematic diagram of the unit cell of the newly developed honeycomb (Type I) under uniaxial *x*- and *y*- directional external stress; (b) analytical model for the slant wall BD; (c) analytical model for the curved wall AB.

One can find from Fig.2 (a) that, points B and C are located in the same plane of symmetry, and thus, $u_B = u_C$. Another important relation of $v_A - v_D = v_B$ can also be obtained according to the symmetry of the structure. It's easy for us to calculate the axial force of walls AD and BC:

$$F_{AD}^a = F_{BC}^a = \frac{E_0 A_0}{h_0} \cdot v_B, \tag{2}$$

where E_0 is the Young's modulus of the basic material; $A_0 = Ht_0$ and H is the height of the wall along the out-of-plane direction. Obviously, there is no shear force acting on the walls AD and BC. Only isotropic basic material was considered in this paper, thus the Yong's modulus (E_0), Poisson's ratio (ν_0) and shear modulus (G_0) satisfy $G_0 = E_0/(2+2\nu_0)$. In addition, to facilitate the analysis, both the basic re-entrant cell and the curved inserts are supposed to be made with the same basic

material in this study, although different basic materials can be respectively used for them in manufacturing to enhance the design flexibility.

Using the force method, the axial and shear forces (F_{BD}^{a} and F_{BD}^{s}) acting on the wall BD can be derived. Taking the wall BD in Fig.2(a) as a statically indeterminate system with three degree of indeterminacy, we obtained a primary structure (a statically determinate system, as shown in Fig.2(b)) by removing three excess restraints and took the reactions as the redundant forces $X_i\left(i=1,2,3\right)$. For facilitating analysis, we established a local rectangular coordinate system, $x'-y'$, in which the x' axis is parallel to the axial direction of the wall BD. Assuming the displacement of point B along the x' direction is $\Delta x'$ while that is $\Delta y'$ along the y' direction. Without loss of generality, we considered the rotation angle at both endpoints of the wall BD, and φ_{B}, φ_{D} is identified to be the positive rotation (clockwise) at points B and D, respectively. The redundant forces $X_i\left(i=1,2,3\right)$ can be attained according to displacement conformability conditions:

$$\begin{cases} \delta_{11}X_1+\delta_{12}X_2+\delta_{13}X_3=\Delta y'-l_0\varphi_{\mathrm{D}}, \\ \delta_{21}X_2+\delta_{22}X_2+\delta_{23}X_3=\Delta x', \\ \delta_{31}X_1+\delta_{32}X_2+\delta_{33}X_3=\varphi_{\mathrm{B}}-\varphi_{\mathrm{D}}, \end{cases} \tag{3}$$

where $\delta_{ij}=\int\frac{M_iM_j}{E_0I_0}+\frac{N_iN_j}{E_0A_0}+\frac{\kappa V_iV_j}{G_0A_0},\left(i,j=1,2,3\right)$; M_i, N_i and V_i is the bending moment, axial force and shear force due to the unit force (X_i=1) applied at B, respectively; $I_0=Ht_0^3/12$ is the second moment of inertia of the wall BD; κ is the geometrical factor and $\kappa=6/5$ for a rectangular cross section. Then, δ_{ij} are given as follows:

$$\begin{aligned} &\delta_{11}=\frac{l_0^3}{3E_0I_0}+\frac{\kappa l_0}{G_0A_0},\delta_{12}=\delta_{21}=0,\delta_{13}=\delta_{31}=\frac{l_0^2}{2E_0I_0}, \\ &\delta_{22}=\frac{l_0}{E_0A_0},\delta_{23}=\delta_{32}=0,\delta_{33}=\frac{l_0}{E_0I_0}. \end{aligned} \tag{4}$$

By substituting Eq.(4) into Eq.(3), we have:

$$X_1 = -\frac{6}{l_0^2/(E_0I_0)+12\kappa/(G_0A_0)}\varphi_B - \frac{6}{l_0^2/(E_0I_0)+12\kappa/(G_0A_0)}\varphi_D + \frac{12\Delta y'}{l_0^3/(E_0I_0)+12\kappa l_0/(G_0A_0)},$$
$$X_2 = \frac{E_0A_0}{l_0}\Delta x',$$
$$X_3 = \left[\frac{3l_0}{l_0^2/(E_0I_0)+12\kappa/(G_0A_0)} + \frac{E_0I_0}{l_0}\right]\varphi_B + \left[\frac{3l_0}{l_0^2/(E_0I_0)+12\kappa/(G_0A_0)} - \frac{E_0I_0}{l_0}\right]\varphi_D - \frac{6\Delta y'}{l_0^2/(E_0I_0)+12\kappa/(G_0A_0)}.$$

(5)

According to the symmetry of the structure, there is no rotation at the points B and D, i.e. $\varphi_B = \varphi_D = 0$ in Eq.(5). From Fig.2(a) and (b), we can get a relation as:

$$\begin{aligned}\Delta x' &= u_B\cos\theta_0 + (v_B - v_D)\sin\theta_0,\\ \Delta y' &= (v_B - v_D)\cos\theta_0 - u_B\sin\theta_0.\end{aligned} \tag{6}$$

By substituting Eq.(6) into Eq.(5), the axial and shear forces (F_{BD}^a and F_{BD}^s) of the wall BD are obtained:

$$\begin{aligned}F_{BD}^a &= HE_0(a_1v_B - a_1v_D + a_2u_B),\\ F_{BD}^s &= HE_0(s_1v_B - s_1v_D + s_2u_B).\end{aligned} \tag{7}$$

where

$$a_1 = t_0\sin\theta_0/l_0,\ a_2 = t_0\cos\theta_0/l_0,$$
$$s_1 = \frac{\cos\theta_0}{l_0^3/t_0^3 + 2\kappa l_0(1+\nu_0)/t_0},\ s_2 = -\frac{\sin\theta_0}{l_0^3/t_0^3 + 2\kappa l_0(1+\nu_0)/t_0}.$$

For the curved wall AB, as shown in Fig.2(c), we established another local rectangular coordinate system, $\xi-\eta$, in which the ξ axis is parallel to the auxiliary chord AB. In Fig.2(c), the positive rotation at points A and B is φ_A and φ_B, respectively; $\Delta\xi$ is the ξ- directional displacement of B while $\Delta\eta$ is the η-directional displacement. We introduced an auxiliary parameter of α_0 in Fig.2(c) for facilitating the analysis. Apparently, α_0 is the central angle subtended by the arc AB

and $\alpha_0 = \arcsin\left[l_1/(2R)\right]$. Similarly, the redundant forces $X_i'(i=1,2,3)$ can be obtained by using the displacement conformability conditions [45]:

$$\begin{cases} \delta_{11}'\mathrm{X}_1' + \delta_{12}'\mathrm{X}_2' + \delta_{13}'\mathrm{X}_3' = \Delta\eta - 2R\sin\beta\varphi_{\mathrm{A}}, \\ \delta_{21}'\mathrm{X}_1' + \delta_{22}'\mathrm{X}_2' + \delta_{23}'\mathrm{X}_3' = \Delta\xi, \\ \delta_{31}'\mathrm{X}_1' + \delta_{32}'\mathrm{X}_2' + \delta_{33}'\mathrm{X}_3' = \varphi_{\mathrm{B}} - \varphi_{\mathrm{A}}, \end{cases} \tag{8}$$

where δ_{ij}' can be calculated as:

$$\begin{aligned}
&\delta_{11}' = \int_0^{\alpha_0} \frac{RM_1' \cdot M_1'}{E_0 I_1} d\beta + \int_0^{\alpha_0} \frac{RN_1' \cdot N_1'}{E_0 A_1} d\beta + \int_0^{\alpha_0} \frac{\kappa RV_1' \cdot V_1'}{G_0 A_1} d\beta + \\
&\int_{\alpha_0}^{2\alpha_0} \frac{RM_1'' \cdot M_1''}{E_0 I_1} d\beta + \int_{\alpha_0}^{2\alpha_0} \frac{RN_1'' \cdot N_1''}{E_0 A_1} d\beta + \int_{\alpha_0}^{2\alpha_0} \frac{\kappa RV_1'' \cdot V_1''}{G_0 A_1} d\beta = \frac{R^3 b}{E_0 I_1} + \frac{Rd}{E_0 A_1} + \frac{\kappa eR}{G_0 A_1}; \\
&\delta_{21}' = \delta_{12}' = \int_0^{\alpha_0} \frac{RM_1' \cdot M_2'}{E_0 I_1} d\beta + \int_0^{\alpha_0} \frac{RN_1' \cdot N_2'}{E_0 A_1} d\beta + \int_0^{\alpha_0} \frac{\kappa RV_1' \cdot V_2'}{G_0 A_1} d\beta + \\
&\int_{\alpha_0}^{2\alpha_0} \frac{RM_1'' \cdot M_2''}{E_0 I_1} d\beta + \int_{\alpha_0}^{2\alpha_0} \frac{RN_1'' \cdot N_2''}{E_0 A_1} d\beta + \int_{\alpha_0}^{2\alpha_0} \frac{\kappa RV_1'' \cdot V_2''}{G_0 A_1} d\beta = \frac{2cR^3 \sin\alpha_0}{E_0 I_1}; \\
&\delta_{13}' = \delta_{31}' = \int_0^{\alpha_0} \frac{RM_1' \cdot M_3}{E_0 I_1} d\beta + \int_{\alpha_0}^{2\alpha_0} \frac{RM_1'' \cdot M_3}{E_0 I_1} d\beta = \frac{2R^2 \alpha_0 \sin\alpha_0}{E_0 I_1}; \\
&\delta_{22}' = \int_0^{\alpha_0} \frac{RM_2' \cdot M_2'}{E_0 I_1} d\beta + \int_0^{\alpha_0} \frac{RN_2' \cdot N_2'}{E_0 A_1} d\beta + \int_0^{\alpha_0} \frac{\kappa RV_2' \cdot V_2'}{G_0 A_1} d\beta + \\
&\int_{\alpha_0}^{2\alpha_0} \frac{RM_2'' \cdot M_2''}{E_0 I_1} d\beta + \int_{\alpha_0}^{2\alpha_0} \frac{RN_2'' \cdot N_2''}{E_0 A_1} d\beta + \int_{\alpha_0}^{2\alpha_0} \frac{\kappa RV_2'' \cdot V_2''}{G_0 A_1} d\beta = \frac{R^3 a}{E_0 I_1} + \frac{eR}{E_0 A_1} + \frac{\kappa Rd}{G_0 A_1}; \\
&\delta_{23}' = \delta_{32}' = \int_0^{\alpha_0} \frac{RM_2' \cdot M_3}{E_0 I_1} d\beta + \int_{\alpha_0}^{2\alpha_0} \frac{RM_2'' \cdot M_3}{E_0 I_1} d\beta = \frac{2cR^2}{E_0 I_1}; \\
&\delta_{33}' = \int_0^{2\alpha_0} \frac{RM_3^2}{E_0 I_1} d\beta = \frac{2R\alpha_0}{E_0 I_1}.
\end{aligned} \tag{9}$$

where

$$\begin{aligned}
a &= \alpha_0 + 2\alpha_0 \cos^2\alpha_0 - 3\sin\alpha_0 \cos\alpha_0, \\
b &= \alpha_0 + 2\alpha_0 \sin^2\alpha_0 - \sin\alpha_0 \cos\alpha_0, \\
c &= \alpha_0 \cos\alpha_0 - \sin\alpha_0, \\
d &= \alpha_0 - \sin\alpha_0 \cos\alpha_0, \\
e &= \alpha_0 + \sin\alpha_0 \cos\alpha_0.
\end{aligned} \tag{10}$$

and $I_1 = Ht_1^3/12$ is the second moment of inertia of the curved wall AB; $A_1 = Ht_1$ is

the cross sectional area of AB. M_i' and M_i'', N_i' and N_i'', V_i' and V_i'' are the bending moment, the axial force and the shear force due to the unit force (X_i'=1) applied at B, respectively:

$$\left.\begin{aligned} M_1' &= R\left[\sin\alpha_0 - \sin\left(\alpha_0-\beta\right)\right] \\ N_1' &= \sin\left(\alpha_0-\beta\right) \\ V_1' &= \cos\left(\alpha_0-\beta\right) \\ M_2' &= R\left[\cos\left(\alpha_0-\beta\right) - \cos\alpha_0\right] \\ N_2' &= \cos\left(\alpha_0-\beta\right) \\ V_2' &= \sin\left(\alpha_0-\beta\right) \end{aligned}\right\}, 0 \le \beta \le \alpha_0; \qquad \left.\begin{aligned} M_3 &= 1 \\ N_3 &= 0 \\ V_3 &= 0 \end{aligned}\right\}, 0 \le \beta \le 2\alpha_0; \tag{11}$$

$$\left.\begin{aligned} M_1'' &= R\left[\sin\left(\beta-\alpha_0\right) + \sin\alpha\right] \\ N_1'' &= \sin\left(\beta-\alpha_0\right) \\ V_1'' &= \sin\left(\beta-\alpha_0\right) \\ M_2'' &= R\left[\cos\left(\beta-\alpha_0\right) - \cos\alpha_0\right] \\ N_2'' &= \cos\left(\beta-\alpha_0\right) \\ V_2'' &= \sin\left(\beta-\alpha_0\right) \end{aligned}\right\}, \ \alpha_0 \le \beta \le 2\alpha_0.$$

It should be noted that, β is an intermediate parameter and it is illustrated in Fig.3 for each case.

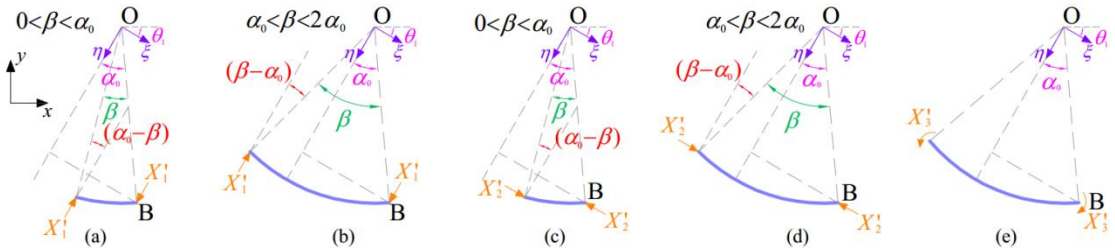

Fig.3. Diagram of the curved wall AB under unit forces $X_i'(i=1,2,3)$.

By substituting the Eqs.(10) and (9) into Eq.(8) , we can obtain the forces X_i' as below:

$$X_1'=\frac{\sin\alpha_0}{R^2\left(2\alpha_0\sin^2\alpha_0-b\right)/\left(E_0I_1\right)-d/\left(E_0A_1\right)-\kappa e/\left(G_0A_1\right)}\left(\varphi_{\mathrm{A}}+\varphi_{\mathrm{B}}\right)-\frac{1}{R^3\left(2\alpha_0\sin^2\alpha_0-b\right)/\left(E_0I_1\right)-Rd/\left(E_0A_1\right)-\kappa eR/\left(G_0A_1\right)}\Delta\eta;$$

$$X_2'=\frac{c}{R^2\left(2c^2-a\alpha_0\right)/\left(E_0I_1\right)-e\alpha_0/\left(E_0A_1\right)-\kappa d\alpha_0/\left(G_0A_1\right)}\left(\varphi_{\mathrm{B}}-\varphi_{\mathrm{A}}\right)-\frac{\alpha_0}{R^3\left(2c^2-a\alpha_0\right)/\left(E_0I_1\right)-e\alpha_0R/\left(E_0A_1\right)-\kappa dR\alpha_0/\left(G_0A_1\right)}\Delta\xi;$$

$$X_3'=\left[-\frac{E_0I_1}{2R\alpha_0}+\frac{Rc^2}{\alpha_0R^2\left(2c^2-a\alpha_0\right)/\left(E_0I_1\right)-e\alpha_0^2/\left(E_0A_1\right)-\kappa d\alpha_0^2/\left(G_0A_1\right)}-\frac{R\sin^2\alpha_0}{R^2\left(2\alpha_0\sin^2\alpha_0-b\right)/\left(E_0I_1\right)-d/\left(E_0A_1\right)-\kappa e/\left(G_0A_1\right)}\right]\varphi_{\mathrm{A}}+\left[\frac{E_0I_1}{2R\alpha_0}-\frac{Rc^2}{\alpha_0R^2\left(2c^2-a\alpha_0\right)/\left(E_0I_1\right)-e\alpha_0^2/\left(E_0A_1\right)-\kappa d\alpha_0^2/\left(G_0A_1\right)}-\frac{R\sin^2\alpha_0}{R^2\left(2\alpha_0\sin^2\alpha_0-b\right)/\left(E_0I_1\right)-d/\left(E_0A_1\right)-\kappa e/\left(G_0A_1\right)}\right]\varphi_{\mathrm{B}}+\frac{c}{R^2\left(2c^2-a\alpha_0\right)/\left(E_0I_1\right)-e\alpha_0/\left(E_0A_1\right)-\kappa d\alpha_0/\left(G_0A_1\right)}\Delta\xi+\frac{\sin\alpha_0}{R^2\left(2\alpha_0\sin^2\alpha_0-b\right)/\left(E_0I_1\right)-d/\left(E_0A_1\right)-\kappa e/\left(G_0A_1\right)}\Delta\eta.$$

(12)

The rotation at points A and B are all equal to zero due to the symmetry, i.e., $\varphi_{\mathrm{A}}=\varphi_{\mathrm{B}}=0$ in Eq.(12). From Fig.2(a) and (c), we have:

$$\begin{aligned}\Delta\xi&=\mathrm{u_B}\cos\theta_1-\left(\mathrm{v_B}-\mathrm{v_A}\right)\sin\theta_1=\mathrm{u_B}\cos\theta_1+\mathrm{v_D}\sin\theta_1,\\ \Delta\eta&=\mathrm{u_B}\sin\theta_1+\left(\mathrm{v_B}-\mathrm{v_A}\right)\cos\theta_1=\mathrm{u_B}\sin\theta_1-\mathrm{v_D}\cos\theta_1.\end{aligned}\tag{13}$$

By substituting Eq.(13) into Eq.(12), the component of the internal forces of the curved wall AB along the ξ and η axes can be expressed as:

$$\begin{aligned}F_{\mathrm{AB}}^{\xi}&=HE_0\left(\xi_1\mathrm{v_D}+\xi_2\mathrm{u_B}\right),\\ F_{\mathrm{AB}}^{\eta}&=HE_0\left(\eta_1\mathrm{v_D}+\eta_2\mathrm{u_B}\right).\end{aligned}\tag{14}$$

where

$$\xi_1=\frac{-\alpha_0\sin\theta_1}{12R^3\left(2c^2-a\alpha_0\right)/t_1^3-e\alpha_0R/t_1-2\kappa dR\alpha_0\left(1+\nu_0\right)/t_1},$$
$$\xi_2=\frac{-\alpha_0\cos\theta_1}{12R^3\left(2c^2-a\alpha_0\right)/t_1^3-e\alpha_0R/t_1-2\kappa dR\alpha_0\left(1+\nu_0\right)/t_1},$$
$$\eta_1=\frac{\cos\theta_1}{12R^3\left(2\alpha_0\sin^2\alpha_0-b\right)/t_1^3-Rd/t_1-2\kappa eR\left(1+\nu_0\right)/t_1},$$
$$\eta_2=\frac{-\sin\theta_1}{12R^3\left(2\alpha_0\sin^2\alpha_0-b\right)/t_1^3-Rd/t_1-2\kappa eR\left(1+\nu_0\right)/t_1}.$$

The component of the internal forces of the curved wall CD along the ξ and η directions is respectively equal to that of the curved wall AB due to the symmetry of the unit cell, i.e., $F_{\mathrm{AB}}^{\xi}=F_{\mathrm{CD}}^{\xi}$ and $F_{\mathrm{AB}}^{\eta}=F_{\mathrm{CD}}^{\eta}$.

(a) E_x^{I} and ν_{xy}^{I}

We first calculated the Yong's modulus (E_x^I) and Poisson's ratio (ν_{xy}^I) of the new honeycomb in Type I, when loading along the *x* direction. The key idea to obtain the effective modulus is using the displacement method to express both the *x*- directional effective stress and strain (σ_x^I and ε_x^I) as a known function of $\mathrm{u_B}$.

Based on the force balance at point B along the *y* direction, i.e., $\Sigma F_{\mathrm{B}y}=0$, it is obtained:

$$F_{\mathrm{BC}}^a+F_{\mathrm{BD}}^a\sin\theta_0+F_{\mathrm{BD}}^s\cos\theta_0+F_{\mathrm{AB}}^{\eta}\cos\theta_1-F_{\mathrm{AB}}^{\xi}\sin\theta_1=0. \tag{15}$$

Since the honeycomb is free along the *y*-direction when the new honeycomb is under *x*- directional uniaxial stress, the total *y*- directional force at point A must be zero. Hence,

$$F_{\mathrm{AD}}^a+F_{\mathrm{AB}}^{\xi}\sin\theta_1-F_{\mathrm{AB}}^{\eta}\cos\theta_1=0. \tag{16}$$

By solving the coupled Eqs.(15) and (16), we have:

$$\begin{pmatrix}\mathrm{v_B}\\ \mathrm{v_D}\end{pmatrix}=\begin{pmatrix}m_1\\ m_2\end{pmatrix}\mathrm{u_B}, \tag{17}$$

where

$$m_1 = \frac{\begin{array}{l}(\eta_2\cos\theta_1 - \xi_2\sin\theta_1)(\eta_1\cos\theta_1 - \xi_1\sin\theta_1 - s_1\cos\theta_0 - a_1\sin\theta_0) + \\ (\xi_2\sin\theta_1 - \eta_2\cos\theta_1 - s_2\cos\theta_0 - a_2\sin\theta_0)(\eta_1\cos\theta_1 - \xi_1\sin\theta_1)\end{array}}{\begin{array}{l}(t_0/h_0)(\eta_1\cos\theta_1 - \xi_1\sin\theta_1 - s_1\cos\theta_0 - a_1\sin\theta_0) + \\ (\eta_1\cos\theta_1 - \xi_1\sin\theta_1)(t_0/h_0 + a_1\sin\theta_0 + s_1\cos\theta_0)\end{array}},$$

$$m_2 = \frac{\begin{array}{l}(t_0/h_0)(\xi_2\sin\theta_1 - \eta_2\cos\theta_1 - s_2\cos\theta_0 - a_2\sin\theta_0) + \\ (\xi_2\sin\theta_1 - \eta_2\cos\theta_1)(t_0/h_0 + a_1\sin\theta_0 + s_1\cos\theta_0)\end{array}}{\begin{array}{l}(t_0/h_0)(\eta_1\cos\theta_1 - \xi_1\sin\theta_1 - s_1\cos\theta_0 - a_1\sin\theta_0) + \\ (\eta_1\cos\theta_1 - \xi_1\sin\theta_1)(t_0/h_0 + a_1\sin\theta_0 + s_1\cos\theta_0)\end{array}}.$$

The vertical displacement of point A can be given as:

$$\mathrm{v_A} = \mathrm{v_B} + \mathrm{v_D} = (m_1 + m_2)\,\mathrm{u_B}. \tag{18}$$

An *x*- directional force balance on the right boundary of the unit cell is established:

$$\sigma_x^{\mathrm{I}}(h_0 - l_0\sin\theta_0)H = F_{\mathrm{BD}}^{a}\cos\theta_0 - F_{\mathrm{BD}}^{s}\sin\theta_0 + F_{\mathrm{AB}}^{\xi}\cos\theta_1 + F_{\mathrm{AB}}^{\eta}\sin\theta_1 + F_{\mathrm{CD}}^{\xi}\cos\theta_1 + F_{\mathrm{CD}}^{\eta}\sin\theta_1 \tag{19}$$

By substituting Eqs. (7) and (14) into Eq.(19), we have:

$$\sigma_x^{\mathrm{I}} = \frac{E_0\left[\begin{array}{l}m_1(a_1\cos\theta_0 - s_1\sin\theta_0) + m_2(2\xi_1\cos\theta_1 + 2\eta_1\sin\theta_1 + s_1\sin\theta_0 - a_1\cos\theta_0) \\ +a_2\cos\theta_0 - s_2\sin\theta_0 + 2\xi_2\cos\theta_1 + 2\eta_2\sin\theta_1\end{array}\right]}{h_0 - l_0\sin\theta_0}\mathrm{u_B} \tag{20}$$

The effective strains along the *x* and *y* direction are:

$$\varepsilon_x^{\mathrm{I}} = \frac{\mathrm{u_B}}{l_0\cos\theta_0}\quad , \tag{21}$$

and

$$\varepsilon_y^{\mathrm{I}} = \frac{\mathrm{v_A}}{h_0 - l_0\sin\theta_0} = \frac{m_1 + m_2}{h_0 - l_0\sin\theta_0}\mathrm{u_B}\quad , \tag{22}$$

respectively.

Finally, the Young's modulus and Poisson's ratio can be obtained by $E_x^I = \sigma_x^I/\varepsilon_x^I$ and $\nu_{xy}^I = -\varepsilon_y^I/\varepsilon_x^I$ respectively:

$$E_x^{\mathrm{I}}=\frac{E_0\left[\begin{array}{l}m_1\left(a_1\cos\theta_0-s_1\sin\theta_0\right)+m_2\left(2\xi_1\cos\theta_1+2\eta_1\sin\theta_1+s_1\sin\theta_0-a_1\cos\theta_0\right)\\+a_2\cos\theta_0-s_2\sin\theta_0+2\xi_2\cos\theta_1+2\eta_2\sin\theta_1\end{array}\right]l_0\cos\theta_0}{h_0-l_0\sin\theta_0},$$

$$\nu_{xy}^{\mathrm{I}}=-\frac{\left(m_1+m_2\right)l_0\cos\theta_0}{h_0-l_0\sin\theta_0}.$$

(23)

(b) E_y^{I} and ν_{yx}^{I}

The unit cell under a *y*- directional uniaxial stress can refer to Fig.2(a). The internal force for each wall has been derived above. When loading along the *y* direction, Eq.(15) still stands due to the *y*- directional force balance at point B. In addition, the new honeycomb is free along the *x* direction when undergoing a *y*- directional loading, thus,

$$F_{\mathrm{BD}}^{a}\cos\theta_0-F_{\mathrm{BD}}^{s}\sin\theta_0+F_{\mathrm{AB}}^{\xi}\cos\theta_1+F_{\mathrm{AB}}^{\eta}\sin\theta_1+F_{\mathrm{CD}}^{\xi}\cos\theta_1+F_{\mathrm{CD}}^{\eta}\sin\theta_1=0. \quad (24)$$

By solving the coupled Eqs.(15) and (24), we have:

$$\begin{pmatrix}\mathrm{v_B}\\ \mathrm{v_D}\end{pmatrix}=\begin{pmatrix}f_1\\ f_2\end{pmatrix}\mathrm{u_B}, \quad (25)$$

where

$$f_1=\frac{\begin{array}{l}\left(\xi_2\sin\theta_1-a_2\sin\theta_0-s_2\cos\theta_0-\eta_2\cos\theta_1\right)\left(2\xi_1\cos\theta_1+2\eta_1\sin\theta_1+s_1\sin\theta_0-a_1\cos\theta_0\right)-\\\left(s_2\sin\theta_0-a_2\cos\theta_0-2\xi_2\cos\theta_1-2\eta_2\sin\theta_1\right)\left(\eta_1\cos\theta_1-a_1\sin\theta_0-s_1\cos\theta_0-\xi_1\sin\theta_1\right)\end{array}}{\begin{array}{l}\left(t_0/h_0+a_1\sin\theta_0+s_1\cos\theta_0\right)\left(2\xi_1\cos\theta_1+2\eta_1\sin\theta_1+s_1\sin\theta_0-a_1\cos\theta_0\right)+\\\left(\eta_1\cos\theta_1-a_1\sin\theta_0-s_1\cos\theta_0-\xi_1\sin\theta_1\right)\left(s_1\sin\theta_0-a_1\cos\theta_0\right)\end{array}},$$

$$f_2=\frac{\begin{array}{l}\left(t_0/h_0+a_1\sin\theta_0+s_1\cos\theta_0\right)\left(s_2\sin\theta_0-a_2\cos\theta_0-2\xi_2\cos\theta_1-2\eta_2\sin\theta_1\right)+\\\left(s_1\sin\theta_0-a_1\cos\theta_0\right)\left(\xi_2\sin\theta_1-a_2\sin\theta_0-s_2\cos\theta_0-\eta_2\cos\theta_1\right)\end{array}}{\begin{array}{l}\left(t_0/h_0+a_1\sin\theta_0+s_1\cos\theta_0\right)\left(2\xi_1\cos\theta_1+2\eta_1\sin\theta_1+s_1\sin\theta_0-a_1\cos\theta_0\right)+\\\left(\eta_1\cos\theta_1-a_1\sin\theta_0-s_1\cos\theta_0-\xi_1\sin\theta_1\right)\left(s_1\sin\theta_0-a_1\cos\theta_0\right)\end{array}}.$$

The vertical displacement of point A is:

$$\mathrm{v_A}=\mathrm{v_B}+\mathrm{v_D}=\left(f_1+f_2\right)\mathrm{u_B}. \quad (26)$$

Hence, the effective strain in the *y* direction is:

$$\varepsilon_y^{\mathrm{I}}=\frac{\mathrm{v_A}}{h_0-l_0\sin\theta_0}=\frac{f_1+f_2}{h_0-l_0\sin\theta_0}\mathrm{u_B}, \quad (27)$$

while the effective strain along the *x* direction is $\varepsilon_x^{\mathrm{I}}=\mathrm{u_B}/\left(l_0\cos\theta_0\right)$.

Due to the force balance at the top boundary of the unit cell, we have:

$$\sigma_y^{\mathrm{I}} l_0 \cos\theta_0 H = F_{\mathrm{AD}}^{a} + F_{\mathrm{AB}}^{\xi} \sin\theta_1 - F_{\mathrm{AB}}^{\eta} \cos\theta_1 . \tag{28}$$

By substituting Eqs.(2) and (14) into Eq.(28), it is obtained:

$$\sigma_y^{\mathrm{I}} = \frac{E_0 \left[f_1 t_0 / h_0 + \left(\xi_1 \sin\theta_1 - \eta_1 \cos\theta_1\right) f_2 + \left(\xi_2 \sin\theta_1 - \eta_2 \cos\theta_1\right) \right]}{l_0 \cos\theta_0} \mathrm{u_B} . \tag{29}$$

Finally, the Young's modulus and Poisson's ratio when loading along the *y* direction can be calculated as:

$$\begin{aligned} E_y^{\mathrm{I}} &= \frac{E_0 \left[f_1 t_0 / h_0 + \left(\xi_1 \sin\theta_1 - \eta_1 \cos\theta_1\right) f_2 + \left(\xi_2 \sin\theta_1 - \eta_2 \cos\theta_1\right) \right] \left(h_0 - l_0 \sin\theta_0\right)}{\left(f_1 + f_2\right) l_0 \cos\theta_0}, \\ \nu_{yx}^{\mathrm{I}} &= -\frac{h_0 - l_0 \sin\theta_0}{l_0 \cos\theta_0 \left(f_1 + f_2\right)}. \end{aligned} \tag{30}$$

(c) E_x^{II}, ν_{xy}^{II}, E_y^{II} and ν_{yx}^{II}

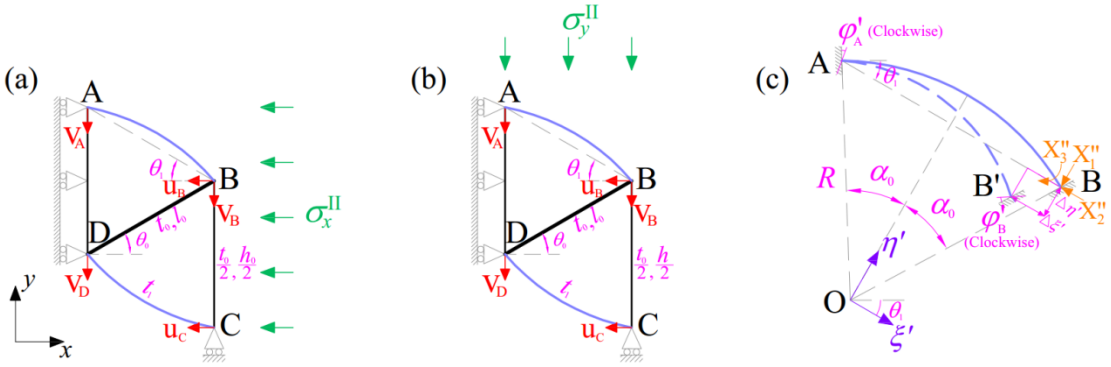

Fig.4. Unit cell of the new honeycomb in Type II: (a) under *x*- directional loading, (b) under *y*-directional loading; (c) free body of diagram of the curved wall AB under forces $X_i''\ (i=1,2,3)$.

Fig.4 (a) and (b) respectively displays the unit cell of the Type II honeycomb under *x*- directional and *y*- directional loading. Displacements of the four key points A, B, C and D are consistent with that illustrated in Fig.2(a). Similarly, the curved wall AB was recognized as a statically indeterminate system with three degree of indeterminacy. We obtained a primary structure, as shown in Fig.4(c), by removing three excess restraints and took the reactions as the redundant forces $X_i''(i=1,2,3)$. φ_{A}' and φ_{B}' are the positive rotation at points A and B, respectively. $\Delta\xi'$ is the

displacement of point B along the ξ' axis of the local rectangular coordinate ξ'-η' while $\Delta\eta'$ is the η'- directional displacement of B.

By using the displacement conformability conditions, the redundant forces $X_i''\ (i=1,2,3)$ can be calculated as:

$$
\begin{aligned}
X_1'' &= \frac{\sin\alpha_0}{R^2\left(2\alpha_0\sin^2\alpha_0-b\right)/\left(E_0I_1\right)-d/\left(E_0A_1\right)-\kappa e/\left(G_0A_1\right)}\left(\varphi_{\mathrm{A}}'+\varphi_{\mathrm{B}}'\right)- \\
&\frac{1}{R^3\left(2\alpha_0\sin^2\alpha_0-b\right)/\left(E_0I_1\right)-Rd/\left(E_0A_1\right)-\kappa eR/\left(G_0A_1\right)}\Delta\eta'; \\
X_2'' &= \frac{c}{R^2\left(2c^2-a\alpha_0\right)/\left(E_0I_1\right)-e\alpha_0/\left(E_0A_1\right)-\kappa d\alpha_0/\left(G_0A_1\right)}\left(\varphi_{\mathrm{A}}'-\varphi_{\mathrm{B}}'\right)- \\
&\frac{\alpha_0}{R^3\left(2c^2-a\alpha_0\right)/\left(E_0I_1\right)-e\alpha_0R/\left(E_0A_1\right)-\kappa dR\alpha_0/\left(G_0A_1\right)}\Delta\xi'; \\
X_3'' &= \left[\begin{array}{c}-\dfrac{E_0I_1}{2R\alpha_0}+\dfrac{Rc^2}{\alpha_0R^2\left(2c^2-a\alpha_0\right)/\left(E_0I_1\right)-e\alpha_0^2/\left(E_0A_1\right)-\kappa d\alpha_0^2/\left(G_0A_1\right)}- \\ \dfrac{R\sin^2\alpha_0}{R^2\left(2\alpha_0\sin^2\alpha_0-b\right)/\left(E_0I_1\right)-d/\left(E_0A_1\right)-\kappa e/\left(G_0A_1\right)}\end{array}\right]\varphi_{\mathrm{A}}'+ \\
&\left[\begin{array}{c}\dfrac{E_0I_1}{2R\alpha_0}-\dfrac{Rc^2}{\alpha_0R^2\left(2c^2-a\alpha_0\right)/\left(E_0I_1\right)-e\alpha_0^2/\left(E_0A_1\right)-\kappa d\alpha_0^2/\left(G_0A_1\right)}- \\ \dfrac{R\sin^2\alpha_0}{R^2\left(2\alpha_0\sin^2\alpha_0-b\right)/\left(E_0I_1\right)-d/\left(E_0A_1\right)-\kappa e/\left(G_0A_1\right)}\end{array}\right]\varphi_{\mathrm{B}}'- \\
&\frac{c}{R^2\left(2c^2-a\alpha_0\right)/\left(E_0I_1\right)-e\alpha_0/\left(E_0A_1\right)-\kappa d\alpha_0/\left(G_0A_1\right)}\Delta\xi'+ \\
&\frac{\sin\alpha_0}{R^2\left(2\alpha_0\sin^2\alpha_0-b\right)/\left(E_0I_1\right)-d/\left(E_0A_1\right)-\kappa e/\left(G_0A_1\right)}\Delta\eta'.
\end{aligned}
\tag{31}
$$

Due to the symmetry of the structure, $\varphi_{\mathrm{A}}'=\varphi_{\mathrm{B}}'=0$ in Eq.(31) when the honeycomb undergoes a uniaxial external stress. Comparing Eq.(31) with Eq.(12), we can find that $X_1'=X_1''$ and $X_2'=X_2''$ when $\varphi_{\mathrm{A}}=\varphi_{\mathrm{B}}=0$ in Eq.(12) and $\varphi_{\mathrm{A}}'=\varphi_{\mathrm{B}}'=0$ in Eq.(31). Consequently, with the same geometric parameters R and t_1, the curved wall AB in Type I honeycomb shows the same internal forces to that in

Type II honeycomb. Based on this, we have:

$$\begin{aligned} E_x^{\mathrm{II}} &= E_x^{\mathrm{I}},\ \nu_{xy}^{\mathrm{II}} = \nu_{xy}^{\mathrm{I}}, \\ E_y^{\mathrm{II}} &= E_y^{\mathrm{I}},\ \nu_{yx}^{\mathrm{II}} = \nu_{yx}^{\mathrm{I}}, \end{aligned} \tag{32}$$

where E_x^{II} and ν_{xy}^{II} are respectively the x- directional effective Young's modulus and Poisson's ratio of the Type II new honeycomb, while E_y^{II} and ν_{yx}^{II} are respectively the y- directional effective Young's modulus and Poisson's ratio of the Type II new honeycomb.

3.1.2. Shear modulus

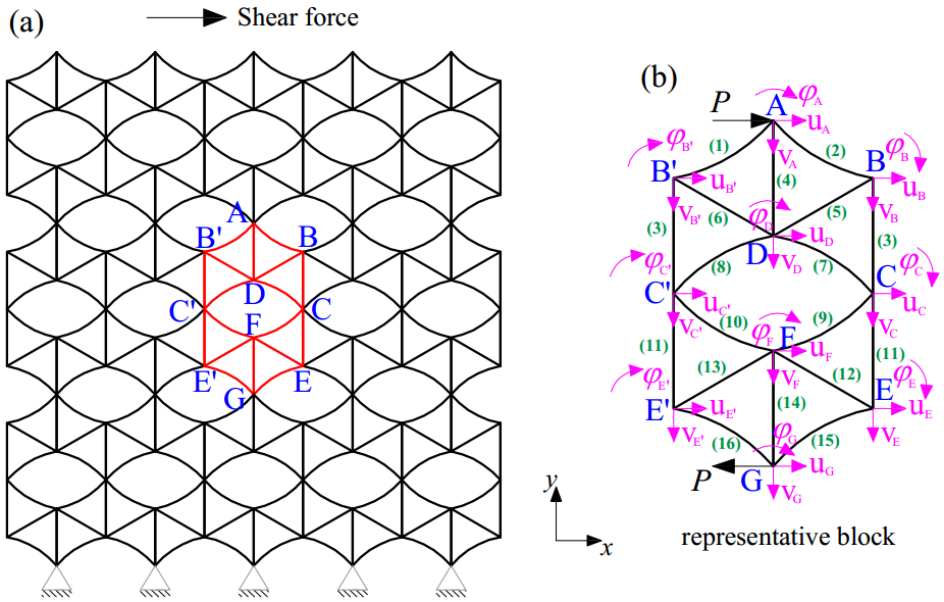

Fig.5. (a) Honeycomb (Type I) under in-plane shear force; (b) free body of diagram of the representative block.

Fig.5 (a) displays the honeycomb (Type I) under an in-plane shear force. According to the symmetry, a representative block, as highlighted in red in Fig.5 (a), was determined. The geometry details for the honeycomb are consistent with that introduced in Section 2. In the representative block, ten key points are contained, i.e., A, B, B′, C, C′, D, E, E′, F and G. The displacements (horizontal displacement, u; vertical displacement, v; rotation, φ) for each point were illustrated in Fig.5(b) in detail. According to the symmetry of the honeycomb, there are three pairs of

symmetric point: points B and B'; points C and C'; points D and D'. Each pair of symmetric point has the same displacements, i.e.,

$$\begin{aligned} &\mathrm{u_B}=\mathrm{u_{B'}},\ \mathrm{v_B}=\mathrm{v_{B'}},\ \varphi_{\mathrm{B}}=\varphi_{\mathrm{B'}};\\ &\mathrm{u_C}=\mathrm{u_{C'}},\ \mathrm{v_C}=\mathrm{v_{C'}},\ \varphi_{\mathrm{C}}=\varphi_{\mathrm{C'}};\\ &\mathrm{u_E}=\mathrm{u_{E'}},\ \mathrm{v_E}=\mathrm{v_{E'}},\ \varphi_{\mathrm{E}}=\varphi_{\mathrm{E'}}. \end{aligned} \tag{33}$$

The main task in the following is to establish relationship between the forces and endpoint displacements for each wall in the representative block.

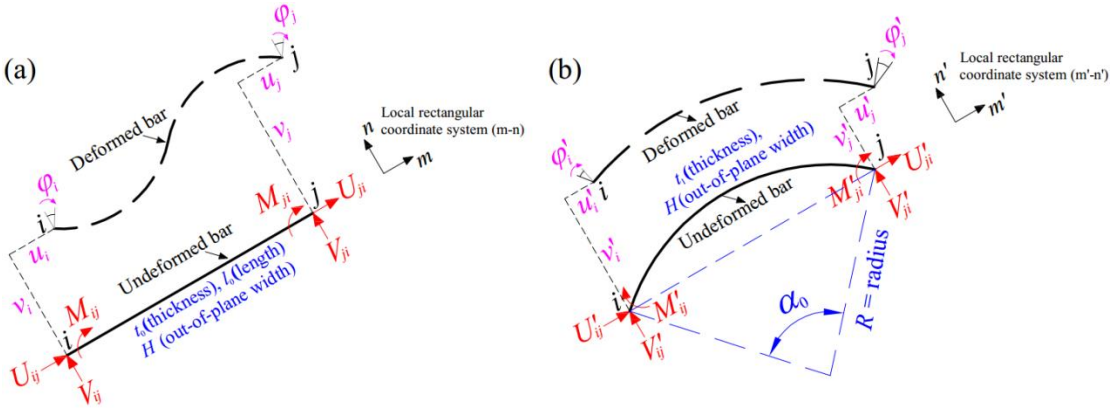

Fig.6. Forces and displacements of a bar: (a) straight bar; (b) arc bar.

Fig.6 shows a generalized model of the straight and arc bars. In Fig.6, several key geometric parameters were identified: H (out-of-plane height), t_0 (thickness of the straight bar), t_1 (thickness of the arc bar), l_0 (length of the straight bar), R (radius of the arc bar) and α_0 (central angle for the arc bar). All the deformations in Fig.6 were described within the local rectangular coordinate systems $m-n$ and $m'-n'$. The axial direction of the straight bar is defined as m axis while that perpendicular to the axial direction is n axis. Analogously, for the arc bar, the axial direction of the auxiliary chord is defined as m' axis. u_i, v_i and φ_i respectively denote the m-directional displacement, n- directional displacement and clockwise rotation of the point i in the straight bar (Fig.6(a)). u_i', v_i' and φ_i' respectively denote the m'-directional displacement, n'- directional displacement and clockwise rotation of the point i in the arc bar (Fig.6(b)).

According to Eq.(5), a generalized relation between the end-point forces

$(U_{ij}, V_{ij}, M_{ij}, U_{ji}, V_{ji}, M_{ji})$ and the end-point displacements $(u_i, v_i, \varphi_i, u_j, v_j, \varphi_j)$ of a straight bar is given as:

$$\mathbf{f^e} = \mathbf{K^e d^e}, \tag{34}$$

where $\mathbf{f^e} = \left(U_{ij}, V_{ij}, M_{ij}, U_{ji}, V_{ji}, M_{ji}\right)^T$, $\mathbf{d^e} = \left(u_i, v_i, \varphi_i, u_j, v_j, \varphi_j\right)^T$ and $\mathbf{K^e}$ is the stiffness matrix of the straight bar that can be given as:

$$\mathbf{K^e} = E_0 \begin{pmatrix} \mathbf{K_{11}} & \mathbf{K_{12}} \\ \mathbf{K_{21}} & \mathbf{K_{22}} \end{pmatrix}, \tag{35}$$

where

$$\mathbf{K_{11}} = \begin{pmatrix} k_{11} & 0 & 0 \\ 0 & k_{22} & k_{23} \\ 0 & k_{23} & k_{33} \end{pmatrix}, \quad \mathbf{K_{12}} = \begin{pmatrix} -k_{11} & 0 & 0 \\ 0 & -k_{22} & k_{23} \\ 0 & -k_{23} & k_{36} \end{pmatrix},$$

$$\mathbf{K_{21}} = \begin{pmatrix} -k_{11} & 0 & 0 \\ 0 & -k_{22} & -k_{23} \\ 0 & k_{23} & k_{36} \end{pmatrix}, \mathbf{K_{22}} = \begin{pmatrix} k_{11} & 0 & 0 \\ 0 & k_{22} & -k_{23} \\ 0 & -k_{23} & k_{33} \end{pmatrix}$$

$$k_{11} = \frac{A_0}{l_0}, k_{22} = \frac{12}{l_0^3/I_0 + 24kl_0(1+\nu_0)/A_0}, k_{23} = \frac{-6}{l_0^2/I_0 + 24k(1+\nu_0)/A_0},$$
$$k_{33} = \frac{3l_0}{l_0^2/I_0 + 24k(1+\nu_0)/A_0} + \frac{I_0}{l_0}, k_{36} = \frac{3l_0}{l_0^2/I_0 + 24k(1+\nu_0)/A_0} - \frac{I_0}{l_0}.$$

Similarly, we can obtain a generalized relation between the forces and displacements of an arc bar by using the Eq. (11):

$$\mathbf{F^e} = \mathbf{G^e D^e}, \tag{36}$$

where $\mathbf{F^e} = \left(U'_{ij}, V'_{ij}, M'_{ij}, U'_{ji}, V'_{ji}, M'_{ji}\right)^T$, $\mathbf{D^e} = \left(u'_i, v'_i, \varphi'_i, u'_j, v'_j, \varphi'_j\right)^T$ and $\mathbf{G^e}$ is the stiffness matrix of the arc bar that can be given as:

$$\mathbf{G^e} = E_0 \begin{pmatrix} \mathbf{G_{11}} & \mathbf{G_{12}} \\ \mathbf{G_{21}} & \mathbf{G_{22}} \end{pmatrix}, \tag{37}$$

where

$$\mathbf{G_{11}} = \begin{pmatrix} g_{11} & 0 & g_{13} \\ 0 & g_{22} & g_{23} \\ g_{13} & g_{23} & g_{33} \end{pmatrix}, \quad \mathbf{G_{12}} = \begin{pmatrix} -g_{11} & 0 & -g_{13} \\ 0 & -g_{22} & g_{23} \\ -g_{13} & -g_{23} & g_{36} \end{pmatrix},$$

$$\mathbf{G_{21}}=\begin{pmatrix}-g_{11} & 0 & -g_{13}\\ 0 & -g_{22} & -g_{23}\\ -g_{13} & g_{23} & g_{36}\end{pmatrix},\quad \mathbf{G_{22}}=\begin{pmatrix}g_{11} & 0 & g_{13}\\ 0 & g_{22} & -g_{23}\\ g_{13} & -g_{23} & g_{33}\end{pmatrix},$$

$$g_{11}=\frac{-\alpha_0}{R^3\left(2c^2-a\alpha_0\right)/I_1-e\alpha_0 R/A_1-2kdR\alpha_0\left(1+\nu_0\right)/A_1};$$

$$g_{13}=\frac{c}{R^2\left(2c^2-a\alpha_0\right)/I_1-e\alpha_0/A_1-2kd\alpha_0\left(1+\nu_0\right)/A_1};$$

$$g_{22}=\frac{-1}{R^3\left(2\alpha_0\sin^2\alpha_0-b\right)/I_1-Rd/A_1-2keR\left(1+\nu_0\right)/A_1};$$

$$g_{23}=\frac{\sin\alpha_0}{R^2\left(2\alpha_0\sin^2\alpha_0-b\right)/I_1-d/A_1-2ke\left(1+\nu_0\right)/A_1};$$

$$g_{33}=\frac{I_1}{2R\alpha_0}-\frac{Rc^2}{\alpha_0R^2\left(2c^2-a\alpha_0\right)/I_1-e\alpha_0^2/A_1-2kd\alpha_0^2\left(1+\nu_0\right)/A_1}-\frac{R\sin^2\alpha_0}{R^2\left(2\alpha_0\sin^2\alpha_0-b\right)/I_1-d/A_1-2ke\left(1+\nu_0\right)/A_1};$$

$$g_{36}=-\frac{I_1}{2R\alpha_0}+\frac{Rc^2}{\alpha_0R^2\left(2c^2-a\alpha_0\right)/I_1-e\alpha_0^2/A_1-2kd\alpha_0^2\left(1+\nu_0\right)/A_1}-\frac{R\sin^2\alpha_0}{R^2\left(2\alpha_0\sin^2\alpha_0-b\right)/I_1-d/A_1-2ke\left(1+\nu_0\right)/A_1}.$$

Thus, the force-displacement equation for each wall in Fig.5(b) can be attained by using Eqs.(34) and (36). The main task in this section is to establish a relation between the shear force *P* and endpoints' displacements (horizontal displacement, u; vertical displacement, v; rotation, φ). To emphasize an important point, the points which are located at the boundary of the representative block, i.e., points B (B'), C (C') and E (E'), are shared by the adjacent representative block. As a result, the effect from the adjacent representative block should be taken into consideration when calculating the resultant force at these points. Thus, the resultant forces at point B (or B') are contributed by the internal forces of the walls AB, BC, BD, AB' and $\mathrm{B}'\mathrm{D}$; the resultant forces at point C (or C') are contributed by the internal forces of the walls DC, BC, CF, CE, $\mathrm{C}'\mathrm{D}$ and FC'; the resultant forces at point E (or E') are contributed by the internal forces of the walls CE, FE, GE, FE' and $\mathrm{E}'\mathrm{G}$.

For the facilitation of analysis, we numbered the walls in Fig.5(b) from (1) to

(16). According to the forces balances at points A, B, C, D, E , F and G, we have:

$$\mathbf{F}^{\mathbf{I}}_{(21\times1)} = \mathbf{Z}^{\mathbf{I}}_{(21\times21)}\mathbf{D}^{\mathbf{I}}_{(21\times1)}, \tag{38}$$

where

$$\mathbf{D}^{\mathbf{I}}_{(21\times1)} = \left(u_A, v_A, \varphi_A, u_B, v_B, \varphi_B, u_C, v_C, \varphi_C, u_D, v_D, \varphi_D, u_E, v_E, \varphi_E, u_F, v_F, \varphi_F, u_G, v_G, \varphi_G\right)^T$$

$$\mathbf{F}^{\mathbf{I}}_{(21\times1)} = \left(F_{Ax}, F_{Ay}, M_A, F_{Bx}, F_{By}, M_B, F_{Cx}, F_{Cy}, M_C, F_{Dx}, F_{Dy}, M_D, F_{Ex}, F_{Ey}, M_E, F_{Fx}, F_{Fy}, M_F, F_{Gx}, F_{Gy}, M_G\right)^T$$

$$= \left(\frac{P}{E_0}, 0, 0, 0, 0, 0, 0, 0, 0, 0, 0, 0, 0, 0, 0, 0, 0, 0, \frac{-P}{E_0}, 0, 0\right)^T$$

$$\mathbf{Z}^{\mathbf{I}}_{(21\times21)} = \begin{pmatrix}
\delta_I^{(1)}G_{11}^{(1)}\lambda_I^{(1)} + \delta_I^{(2)}G_{22}^{(2)}\lambda_I^{(2)} + \delta_I^{(4)}K_{11}^{(4)}\lambda_I^{(4)} & \delta_I^{(1)}G_{12}^{(1)}\lambda_I^{(1)} + \delta_I^{(2)}G_{21}^{(2)}\lambda_I^{(2)} & 0 & \delta_I^{(4)}K_{12}^{(4)}\lambda_I^{(4)} & 0 & 0 & 0 \\
\delta_I^{(1)}G_{21}^{(1)}\lambda_I^{(1)} + \delta_I^{(2)}G_{12}^{(2)}\lambda_I^{(2)} & \delta_I^{(1)}G_{22}^{(1)}\lambda_I^{(1)} + \delta_I^{(2)}G_{11}^{(2)}\lambda_I^{(2)} + \delta_I^{(3)}K_{11}^{(3)}\lambda_I^{(3)} + \delta_I^{(5)}K_{11}^{(5)}\lambda_I^{(5)} + \delta_I^{(6)}K_{11}^{(6)}\lambda_I^{(6)} & \delta_I^{(3)}K_{12}^{(3)}\lambda_I^{(3)} & \delta_I^{(5)}K_{12}^{(5)}\lambda_I^{(5)} + \delta_I^{(6)}K_{12}^{(6)}\lambda_I^{(6)} & 0 & 0 & 0 \\
0 & \delta_I^{(3)}K_{21}^{(3)}\lambda_I^{(3)} & \delta_I^{(3)}K_{22}^{(3)}\lambda_I^{(3)} + \delta_I^{(7)}G_{22}^{(7)}\lambda_I^{(7)} + \delta_I^{(8)}G_{11}^{(8)}\lambda_I^{(8)} + \delta_I^{(9)}G_{11}^{(9)}\lambda_I^{(9)} + \delta_I^{(10)}G_{22}^{(10)}\lambda_I^{(10)} + \delta_I^{(11)}K_{11}^{(11)}\lambda_I^{(11)} & \delta_I^{(7)}G_{21}^{(7)}\lambda_I^{(7)} + \delta_I^{(8)}G_{12}^{(8)}\lambda_I^{(8)} & \delta_I^{(11)}K_{12}^{(11)}\lambda_I^{(11)} & \delta_I^{(9)}G_{12}^{(9)}\lambda_I^{(9)} + \delta_I^{(10)}G_{21}^{(10)}\lambda_I^{(10)} & 0 \\
\delta_I^{(4)}K_{21}^{(4)}\lambda_I^{(4)} & \delta_I^{(5)}K_{21}^{(5)}\lambda_I^{(5)} + \delta_I^{(6)}K_{21}^{(6)}\lambda_I^{(6)} & \delta_I^{(7)}G_{12}^{(7)}\lambda_I^{(7)} + \delta_I^{(8)}G_{21}^{(8)}\lambda_I^{(8)} & \delta_I^{(4)}K_{22}^{(4)}\lambda_I^{(4)} + \delta_I^{(5)}K_{22}^{(5)}\lambda_I^{(5)} + \delta_I^{(6)}K_{22}^{(6)}\lambda_I^{(6)} + \delta_I^{(7)}G_{11}^{(7)}\lambda_I^{(7)} + \delta_I^{(8)}G_{22}^{(8)}\lambda_I^{(8)} & 0 & 0 & 0 \\
0 & 0 & \delta_I^{(11)}K_{21}^{(11)}\lambda_I^{(11)} & 0 & \delta_I^{(11)}K_{22}^{(11)}\lambda_I^{(11)} + \delta_I^{(12)}K_{22}^{(12)}\lambda_I^{(12)} + \delta_I^{(13)}K_{22}^{(13)}\lambda_I^{(13)} + \delta_I^{(15)}G_{22}^{(15)}\lambda_I^{(15)} + \delta_I^{(16)}G_{11}^{(16)}\lambda_I^{(16)} & \delta_I^{(12)}K_{21}^{(12)}\lambda_I^{(12)} + \delta_I^{(13)}K_{21}^{(13)}\lambda_I^{(13)} & \delta_I^{(15)}G_{21}^{(15)}\lambda_I^{(15)} + \delta_I^{(16)}G_{12}^{(16)}\lambda_I^{(16)} \\
0 & 0 & \delta_I^{(9)}G_{21}^{(9)}\lambda_I^{(9)} + \delta_I^{(10)}G_{12}^{(10)}\lambda_I^{(10)} & 0 & \delta_I^{(12)}K_{12}^{(12)}\lambda_I^{(12)} + \delta_I^{(13)}K_{12}^{(13)}\lambda_I^{(13)} & \delta_I^{(9)}G_{22}^{(9)}\lambda_I^{(9)} + \delta_I^{(10)}G_{11}^{(10)}\lambda_I^{(10)} + \delta_I^{(12)}K_{11}^{(12)}\lambda_I^{(12)} + \delta_I^{(13)}K_{11}^{(13)}\lambda_I^{(13)} + \delta_I^{(14)}K_{11}^{(14)}\lambda_I^{(14)} & \delta_I^{(14)}K_{12}^{(14)}\lambda_I^{(14)} \\
0 & 0 & 0 & 0 & \delta_I^{(15)}G_{12}^{(15)}\lambda_I^{(15)} + \delta_I^{(16)}G_{21}^{(16)}\lambda_I^{(16)} & \delta_I^{(14)}K_{21}^{(14)}\lambda_I^{(14)} & \delta_I^{(14)}K_{22}^{(14)}\lambda_I^{(14)} + \delta_I^{(15)}G_{11}^{(15)}\lambda_I^{(15)} + \delta_I^{(16)}G_{22}^{(16)}\lambda_I^{(16)}
\end{pmatrix}$$

$$\boldsymbol{\lambda}_{\mathbf{I}}^{(1)} = \boldsymbol{\lambda}_{\mathbf{I}}^{(9)} = \begin{pmatrix} -\cos\theta_1 & \sin\theta_1 & 0 \\ \sin\theta_1 & \cos\theta_1 & 0 \\ 0 & 0 & 1 \end{pmatrix}, \boldsymbol{\delta}_{\mathbf{I}}^{(1)} = \boldsymbol{\delta}_{\mathbf{I}}^{(9)} = \left(\boldsymbol{\lambda}_{\mathbf{I}}^{(1)}\right)^{-1} = \begin{pmatrix} -\cos\theta_1 & \sin\theta_1 & 0 \\ \sin\theta_1 & \cos\theta_1 & 0 \\ 0 & 0 & 1 \end{pmatrix};$$

$$\boldsymbol{\lambda}_{\mathbf{I}}^{(2)} = \boldsymbol{\lambda}_{\mathbf{I}}^{(10)} = \begin{pmatrix} -\cos\theta_1 & -\sin\theta_1 & 0 \\ -\sin\theta_1 & \cos\theta_1 & 0 \\ 0 & 0 & 1 \end{pmatrix}, \boldsymbol{\delta}_{\mathbf{I}}^{(2)} = \boldsymbol{\delta}_{\mathbf{I}}^{(10)} = \left(\boldsymbol{\lambda}_{\mathbf{I}}^{(2)}\right)^{-1} = \begin{pmatrix} -\cos\theta_1 & -\sin\theta_1 & 0 \\ -\sin\theta_1 & \cos\theta_1 & 0 \\ 0 & 0 & 1 \end{pmatrix};$$

$$\boldsymbol{\lambda}_{\mathbf{I}}^{(3)} = \boldsymbol{\lambda}_{\mathbf{I}}^{(4)} = \boldsymbol{\lambda}_{\mathbf{I}}^{(11)} = \boldsymbol{\lambda}_{\mathbf{I}}^{(14)} = \begin{pmatrix} 0 & 1 & 0 \\ 1 & 0 & 0 \\ 0 & 0 & 1 \end{pmatrix}, \boldsymbol{\delta}_{\mathbf{I}}^{(3)} = \boldsymbol{\delta}_{\mathbf{I}}^{(4)} = \boldsymbol{\delta}_{\mathbf{I}}^{(11)} = \boldsymbol{\delta}_{\mathbf{I}}^{(14)} = \left(\boldsymbol{\lambda}_{\mathbf{I}}^{(3)}\right)^{-1} = \begin{pmatrix} 0 & 1 & 0 \\ 1 & 0 & 0 \\ 0 & 0 & 1 \end{pmatrix};$$

$$\boldsymbol{\lambda}_{\mathbf{I}}^{(5)} = \boldsymbol{\lambda}_{\mathbf{I}}^{(13)} = \begin{pmatrix} -\cos\theta_0 & \sin\theta_0 & 0 \\ \sin\theta_0 & \cos\theta_0 & 0 \\ 0 & 0 & 1 \end{pmatrix}, \boldsymbol{\delta}_{\mathbf{I}}^{(5)} = \boldsymbol{\delta}_{\mathbf{I}}^{(13)} = \left(\boldsymbol{\lambda}_{\mathbf{I}}^{(5)}\right)^{-1} = \begin{pmatrix} -\cos\theta_0 & \sin\theta_0 & 0 \\ \sin\theta_0 & \cos\theta_0 & 0 \\ 0 & 0 & 1 \end{pmatrix};$$

$$\boldsymbol{\lambda}_{\mathbf{I}}^{(6)} = \boldsymbol{\lambda}_{\mathbf{I}}^{(12)} = \begin{pmatrix} \cos\theta_0 & \sin\theta_0 & 0 \\ \sin\theta_0 & -\cos\theta_0 & 0 \\ 0 & 0 & 1 \end{pmatrix}, \boldsymbol{\delta}_{\mathbf{I}}^{(6)} = \boldsymbol{\delta}_{\mathbf{I}}^{(12)} = \left(\boldsymbol{\lambda}_{\mathbf{I}}^{(6)}\right)^{-1} = \begin{pmatrix} \cos\theta_0 & \sin\theta_0 & 0 \\ \sin\theta_0 & -\cos\theta_0 & 0 \\ 0 & 0 & 1 \end{pmatrix};$$

$$\boldsymbol{\lambda}_{\mathbf{I}}^{(7)}=\boldsymbol{\lambda}_{\mathbf{I}}^{(16)}=\begin{pmatrix}\cos\theta_1 & \sin\theta_1 & 0\\ \sin\theta_1 & -\cos\theta_1 & 0\\ 0 & 0 & 1\end{pmatrix},\boldsymbol{\delta}_{\mathbf{I}}^{(7)}=\boldsymbol{\delta}_{\mathbf{I}}^{(16)}=\left(\boldsymbol{\lambda}_{\mathbf{I}}^{(7)}\right)^{-1}=\begin{pmatrix}\cos\theta_1 & \sin\theta_1 & 0\\ \sin\theta_1 & -\cos\theta_1 & 0\\ 0 & 0 & 1\end{pmatrix};$$

$$\boldsymbol{\lambda}_{\mathbf{I}}^{(8)}=\boldsymbol{\lambda}_{\mathbf{I}}^{(15)}=\begin{pmatrix}\cos\theta_1 & -\sin\theta_1 & 0\\ -\sin\theta_1 & -\cos\theta_1 & 0\\ 0 & 0 & 1\end{pmatrix},\boldsymbol{\delta}_{\mathbf{I}}^{(8)}=\boldsymbol{\delta}_{\mathbf{I}}^{(15)}=\left(\boldsymbol{\lambda}_{\mathbf{I}}^{(8)}\right)^{-1}=\begin{pmatrix}\cos\theta_1 & -\sin\theta_1 & 0\\ -\sin\theta_1 & -\cos\theta_1 & 0\\ 0 & 0 & 1\end{pmatrix}.$$

In the force matrix $\mathbf{F}_{(21\times1)}^{\mathbf{I}}$, F_{ix}, F_{iy}, M_i respectively denote the x- component force, y- component force and bending moment at point i. In the matrix $\mathbf{Z}_{(21\times21)}^{\mathbf{I}}$, $\mathbf{K}_{\mathbf{mn}}^{(\mathbf{k})}$ and $\mathbf{G}_{\mathbf{mn}}^{(\mathbf{k})}$ $(\mathbf{m}=1,2;\mathbf{n}=1,2)$ are the component of the stiffness matrix of the cell wall $\mathbf{k}$ in Fig.5(b), which can be obtained from Eq. (34) and Eq.(36), respectively. $\boldsymbol{\delta}_{\mathbf{I}}^{\mathbf{k}}$ is the coordinate transformation matrix from the local coordinate to the global coordinate (the Cartesian coordinates of x-y in Fig.5(b)), while $\boldsymbol{\lambda}_{\mathbf{I}}^{\mathbf{k}}$ denotes the coordinate transformation matrix from the global coordinate to the local coordinate. In a straight wall, the local coordinate refers to the rectangular coordinate system formed by the axial direction and its perpendicular direction, while for the curved wall, the local coordinate is formed by the axial direction of the chord and its perpendicular direction, example being the local rectangular coordinate system $m-n$ and $m'-n'$ plotted in Fig.6.

From Eq.(38), the displacements of all the points can be expressed as a known function of the shear force, P. The shear stress and strain are:

$$\tau_{xy}^{\mathrm{I}}=\frac{P}{2Hl_0\cos\theta_0}\quad , \tag{39}$$

and

$$\gamma_{xy}^{\mathrm{I}}=\frac{\mathrm{u_A}-\mathrm{u_G}}{2\left(h_0-l_0\sin\theta_0\right)}\quad , \tag{40}$$

respectively. Finally, the in-plane shear modulus for the Type I honeycomb is calculated by $G_{xy}^{\mathrm{I}}=\tau_{xy}^{\mathrm{I}}/\gamma_{xy}^{\mathrm{I}}$. The shear modulus of the Type II honeycomb, G_{xy}^{II}, can be obtained by using the similar derivation (see Appendix A).

3.2. Numerical investigations

3.2.1. Finite element (FE) models

Finite element (FE) models for the new honeycombs were built to verify the theoretical predictions of elastic modulus derived in the previous subsection of this paper. Commercially available FE software ANSYS/APDL (version 16.0, ANSYS Inc.) was used to carry out all the simulations in this study. The basic material of the honeycomb block was adopted as the acrylonitrile butadiene styrene (ABS) polymer which is assumed to be elastic, perfectly plastic with $E_0 = 2200\text{MPa}$, $\sigma_{ys} = 31\text{MPa}$, $\nu_0 = 0.35$ and $\rho_0 = 1.05\text{g}\cdot\text{cm}^{-3}$ [43]. Structures' computational design in this study was modeled using the SOLIDWORKS 3D CAD software. All of the FE models satisfy an uniform geometric relation of $H = t_0 = 2t_1$. Once the model was generated, it would be finally imported into ANSYS for analysis and the respective material and its properties would be assigned to the model. 3D models of the new honeycomb blocks (7×5 cells) were meshed using 20-node solid element, Solid 186. A free tetrahedral meshing scheme with an element size of t_1 was used. The FE simulation work done by Harkati et al.[44] was used for reference, and the detailed boundary conditions adopted in the current FE simulations are displayed in Fig.7, in which the Type I honeycomb is used as an example. The same conditions and modeling are also used for the Type II honeycomb. In the case of *x*- directional compression (Fig.7(a)), nodes on the left boundary were constrained along the *x* direction ($\text{u}_x = 0$) while those on the right boundary were applied with a uniform displacement ($-\Delta\text{u}$). The node located in the center of the left boundary were constrained in both *y* and *z* directions to avoid the rigid body displacement. Similarly, the bottom boundary was constrained along the *y* direction while a uniform displacement was applied on the top boundary when compressing along the *y* direction (Fig.7(b)); the node located in the center of the bottom boundary were constrained in both *x* and *z* directions. For the in-plane shear loading (Fig.7(c)), nodes on the top boundary were constrained in both *y* and *z* directions, and an *x*- directional uniform displacement, Δu, was applied on

them; the bottom boundary was fixed ($u_x = 0, u_y = 0$ and $u_z = 0$). What needs to be stressed is that the applied displacement should be small enough to ensure all the analyses are done within the linear elastic region.

In order to minimize the influence of the boundary on the calculation results, the central cell (Fig.7(d)) was chosen to calculate the effective elastic modulus. Forces and average displacement on the surfaces A, B, C and D can be readily attained by using the ANSYS software and thus the effective elastic modulus can be further calculated.

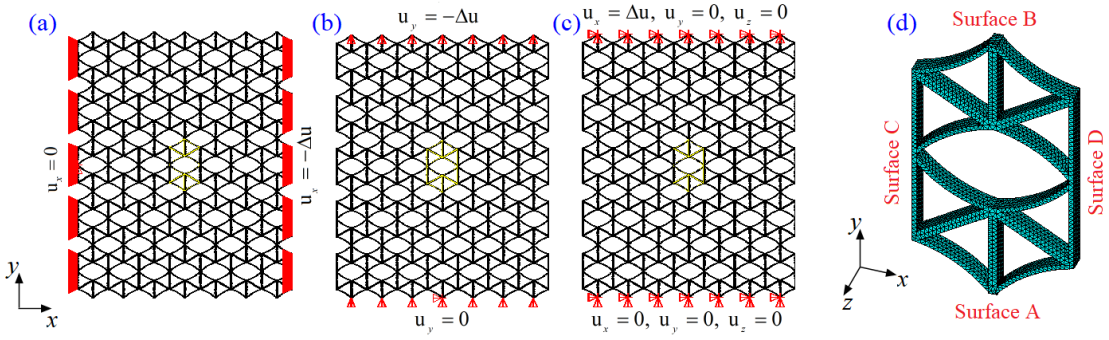

Fig.7. Schematic diagram of the FE model of new honeycomb (Type I) under: (a) *x*- directional compression; (b) *y*- directional compression; (c) in-plane shear; (d) the central cell chose for calculating the effective elastic modulus.

The mesh sensitivity analyses were also conducted in this paper to ensure the accuracy of the proposed meshing scheme. As mentioned above, the mesh size of t_1 was adopted for all of the cases. The maximum value of t_1 (i.e., the maximum mesh size) in this paper is 1.25 mm and hence it would be heavily discussed in the following. Implementing four levels of mesh sizes (0.625mm, 0.8mm, 1mm and 1.25mm) in the new honeycombs (Type I and Type II) with $l_0 = 50\text{mm}$, $h_0 = 100\text{mm}$, $R = 100\text{mm}$, $\theta_0 = 30°$, $H = t_0 = 2.5\text{mm}$ and $t_1 = 1.25\text{mm}$, the total element numbers for the honeycomb models under different mesh sizes were obtained, as illustrated in Table.1. The in-plane elastic moduli of the honeycombs corresponding to different mesh sizes can be calculated by using the proposed numerical procedure, and the results are displayed in Fig. 8 and Fig. 9. One can find that the elastic moduli obtained from 1.25mm mesh size are very close to that obtained from the other lower sizes while the total element number of the honeycomb model with 1.25mm mesh size is much lower than the others, which reveals that 1.25mm mesh size can meet the

accuracy requirement with less computations. As a result, it is to be expected that the proposed meshing scheme with the mesh size of t_1 is suitable for all of the honeycombs.

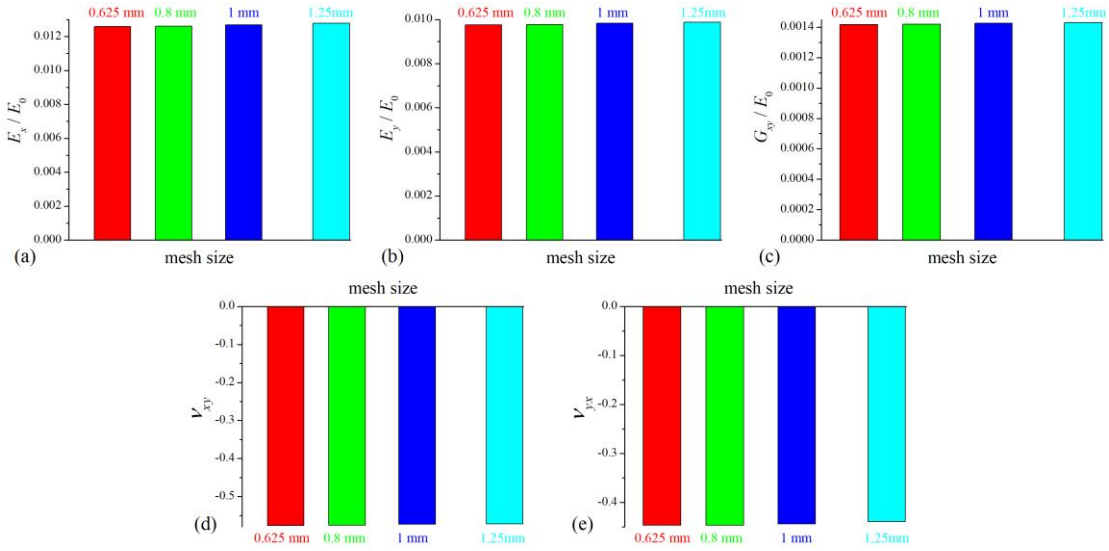

Fig.8. Mesh sensitivity analyses on the in-plane equivalent elastic moduli of the new honeycomb (Type I) with $l_0 = 50\text{mm}$, $h_0 = 100\text{mm}$, R=100mm, $\theta_0 = 30°$, t_0=2.5 mm and $t_1 = 1.25$ mm.

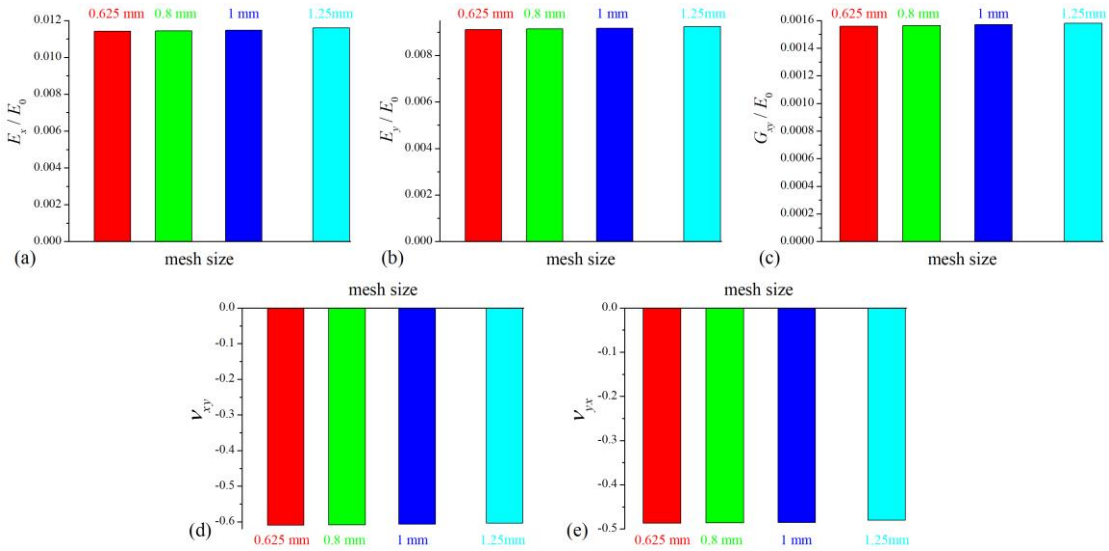

Fig.9. Mesh sensitivity analyses on the in-plane equivalent elastic moduli of the new honeycomb (Type II) with $l_0 = 50\text{mm}$, $h_0 = 100\text{mm}$, R=100mm, $\theta_0 = 30°$, t_0=2.5 mm and $t_1 = 1.25$ mm.

Table 1. Total element numbers of the new honeycomb (both Type I and II) under the tetrahedral meshing scheme with four levels of mesh size (0.625mm, 0.8mm, 1 mm and 1.25mm).

mesh size	total element number	
	new honeycomb (Type I)	new honeycomb (Type II)
0.625 mm	3480037	3485294
0.8 mm	1595410	1642376
1 mm	663428	696907
1.25 mm	421860	407044

3.2.2. FE validations and parameters studies

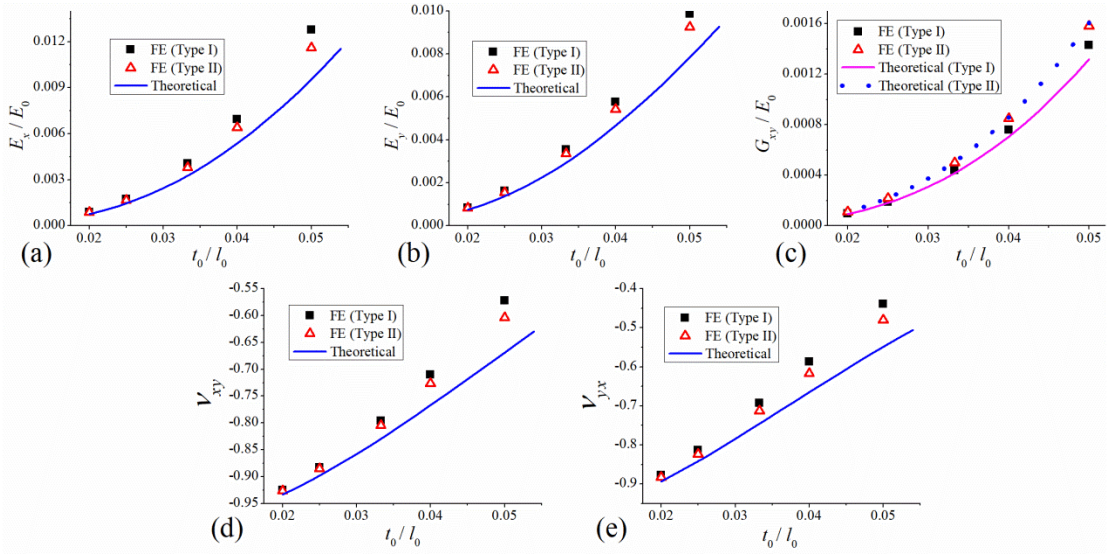

Fig.10. FE and theoretical predictions of the in-plane elastic modulus versus t_0/l_0 while $l_0=50\text{mm}$, $h_0=100\text{mm}$, R=100mm, $\theta_0=30°$, $t_1=0.5t_0$: (a) E_x/E_0; (b) E_y/E_0; (c) G_{xy}/E_0; (d) ν_{xy}; (d) ν_{yx}.

Fig.10 displays the FE and theoretical predictions of in-plane elastic modulus versus t_0/l_0 while $l_0=50\text{mm}$, $h_0=100\text{mm}$, R=100mm, $\theta_0=30°$ and $t_1=0.5t_0$. In the FE models, five levels of t_0/l_0 were obtained by five different values of t_0: t_0=1mm, t_0=1.25mm, t_0=1.66mm, t_0=2mm, and t_0=2.5mm. Comparing the

theoretical predictions with the FE results, a very good agreement can be found between them under small value of t_0/l_0. With t_0/l_0 increasing, the difference between the theoretical and FE results increases progressively. This is because the theoretical models based on the classical beam theory neglect the joint regions of cell walls, while the solid element in FE analysis can fully describe the geometry of structures. The larger t_0/l_0 is, the larger the joint regions and thus the more intensive their influence are. From above analysis, one can draw a conclusion that the theoretical model developed in this paper can offer a good accuracy for the structures with low t_0/l_0.

For further validations, we conducted more FE cases to verify the theoretical models, as shown in Figs.11 and 12. A low value of t_0/l_0=0.02 was adopted in Figs.11 and 12 while the effects of θ_0 and R/l_1 on the effective modulus were demonstrated respectively. Theoretical predictions in Figs.11 and 12 are very close to FE results, which help to verify the theoretical models.

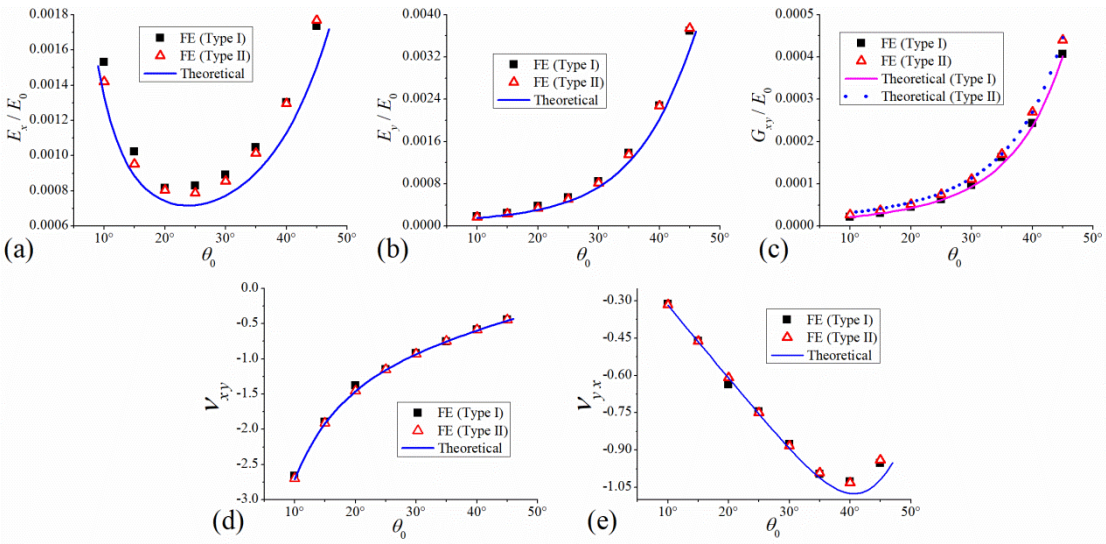

Fig.11. FE and theoretical predictions of the in-plane elastic moduli versus θ_0 while $l_0=50\text{mm}$, $h_0=100\text{mm}$, R=100mm, $t_0=1\text{mm}$, $t_1=0.5\text{mm}$: (a) E_x/E_0; (b) E_y/E_0; (c) G_{xy}/E_0; (d) ν_{xy}; (d) ν_{yx}.

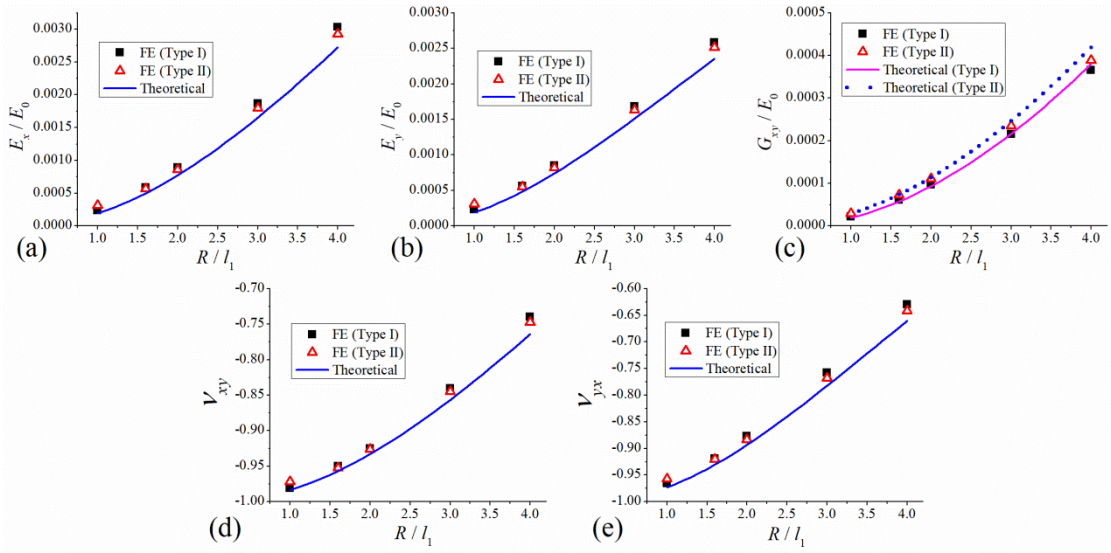

Fig.12. FE and theoretical predictions of the in-plane elastic modulus versus R/l_1 while $l_0 = 50\text{mm}$, $h_0 = 100\text{mm}$, $\theta_0 = 30°$, $t_0 = 1\text{mm}$, $t_1 = 0.5\text{mm}$: (a) E_x/E_0; (b) E_y/E_0; (c) G_{xy}/E_0; (d) v_{xy}; (d) v_{yx}.

For both the Types I and II honeycombs, the dimensionless Young's modulus (E_x/E_0, E_y/E_0) and shear modulus (G_{xy}/E_0) monotonically increase with t_0/l_0 (see Fig.10 (a), (b) and (c)). In Fig.10 (d) and (e), obvious negative value of Poisson's ratio can be found and the NPR effect decreases with t_0/l_0. It is remarkable that the Young's modulus and Poisson's ratios of both types of the new honeycombs are quite close under low t_0/l_0, which is consistent with the theoretical prediction (see Eq.(32)). However, with t_0/l_0 increasing, differences in Young's modulus and Poisson's ratio between the Type I and Type II honeycombs become gradually significant. A reason for this lies in the different joint regions among the walls in the two types of honeycombs. Regarding the in-plane shear modulus, we can find from the theoretical and FE results plotted in Fig.10 (c) that the shear modulus of the Type II honeycomb is slightly larger than that of the Type I honeycomb.

In Fig.11(a), the *x*- directional Young's modulus, E_x/E_0, decreases with θ_0 to a minimum value and then increases. The minimum value occurs at around $\theta_0 = 25°$.

Unlike E_x/E_0, the *y*- directional Young's modulus and shear modulus monotonically increase with θ_0 (see Figs.11(b) and (c)). We can also find that the shear modulus of the Type II honeycomb is slightly higher than that of the Type I honeycomb under the same angle value. For increasing θ_0, the value of ν_{xy} increases while ν_{yx} decreases with θ_0 to a minimum value and then increases. The minimum value of ν_{yx} is observed at around θ_0=40°. Clearly, the slant angle, θ_0, is a quite influential design parameter in altering the auxeticity and stiffness of the structures.

With respect to the existing embedded enhanced auxetic structures, the new honeycombs developed in this paper are best distinguished by the curved insets in them. Looking back to Fig.1 and Eq.(1), a determined length of the auxiliary line (l_1) is attained by any given h_0, l_0 and θ_0. For facilitating the analysis, we introduced a dimensionless parameter R/l_1 to evaluate the bending degree of the curved walls. The large R/l_1, the lower bending degree the curved wall. The curved wall will become straight when $R/l_1 \to \infty$. As we know, axial deformation of the wall will be progressively significant with R/l_1 increasing. In particular, deformation of the curved walls will dramatically affect the dominated deformation mode of the whole structure. Taking an extreme case, when R/l_1 for the walls AB and CD in Fig.2(a) approaches to infinity, the curved profile will transform to be a straight wall and thus two stretching-dominated triangles (ΔABD and ΔCBD) were formed. Consequently, the dominated deformation mode of the structures will change from bending to stretching with R/l_1 increasing. This is the reason for the phenomenon displayed in Fig.12 that the stiffness (E_x/E_0, E_y/E_0, G_{xy}/E_0) of the structures increase (Fig.12 (a), (b) and (c)) while the auxeticity diminishes (Fig.12 (d) and (e)) with R/l_1.

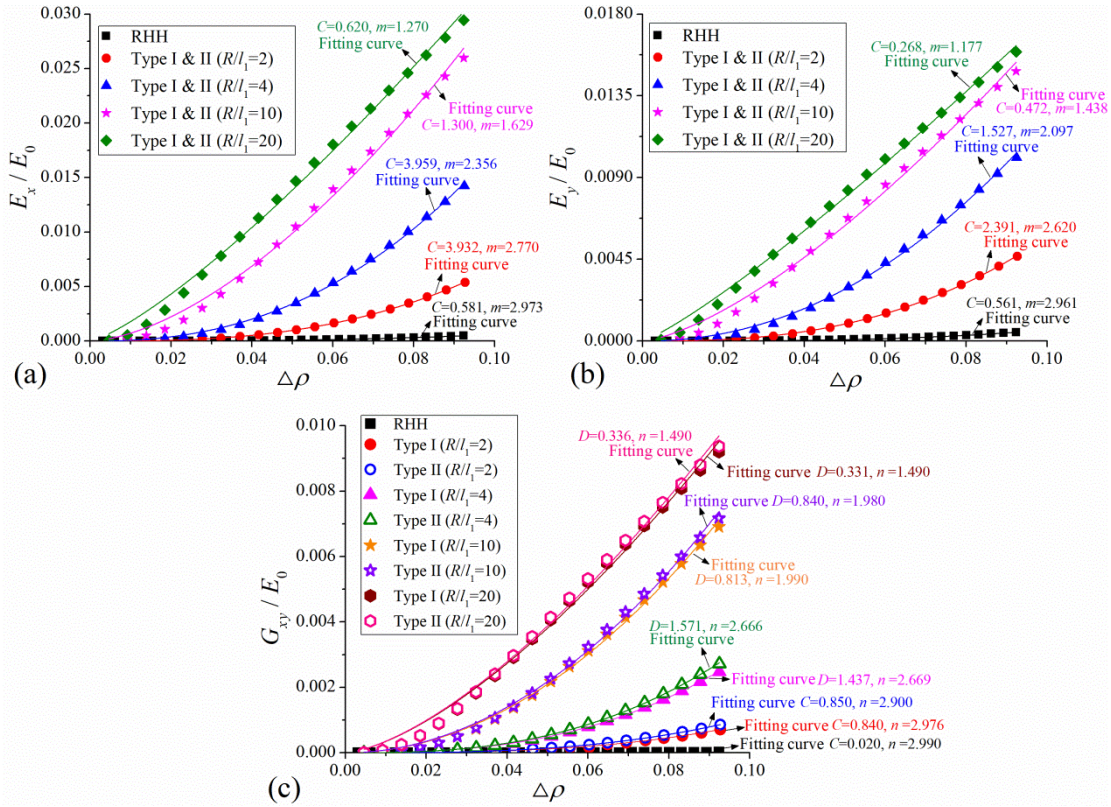

Fig.13. Theoretical predictions of the in-plane elastic modulus of RHH and new honeycombs versus relative density ($\Delta\rho$) for various R/l_1 while $l_0 = 50\text{mm}$, $h_0 = 100\text{mm}$, $\theta_0 = 30°$, $t_1 = 0.5t_0$: (a) E_x/E_0; (b) E_y/E_0; (c) G_{xy}/E_0.

Actually, the dominated deformation mode can be explained by the relation between the Young's modulus and relative density, as illustrated in Fig.13 (a) and (b). The relative density ($\Delta\rho$) of the RHH is calculated as:

$$\Delta\rho = \frac{\rho^*}{\rho_0} = \frac{\left(h_0/l_0 + 2\right)\left(t_0/l_0\right)}{2\left(h_0/l_0 - \sin\theta_0\right)\cos\theta_0} \tag{41}$$

while for the new honeycombs (both Types I and II) , their relative density ($\Delta\rho$) is:

$$\Delta\rho = \frac{\rho^*}{\rho_0} = \frac{t_0 h_0/2 + t_0 l_0 + 4Rt_1 \arcsin\left[l_1/(2R)\right]}{\left(h_0/l_0 - \sin\theta_0\right) l_0 \cos\theta_0} \tag{42}$$

where ρ^* and ρ_0 denote the density of the honeycomb and the bulk material, respectively. It should be noted that Eqs.(41) and (42) are only suitable for honeycombs with low relative density as they neglected the geometry of joint regions.

Therefore, Fig.13 only discussed the honeycombs with relative density lower than 0.1. Various levels of relative densities can be attained by keeping $l_0 = 50\text{mm}$, $h_0 = 100\text{mm}$, $\theta_0 = 30°$, $t_1 = 0.5t_0$ unchanged while varying t_0 from 0.1mm to 3mm. The data plotted in Fig.13 were generated from the numerically validated theoretical models.

It can be seen that both the Young's modulus and shear modulus increase with the relative density. Also, the Young's modulus and shear modulus of the new honeycombs are significantly higher than those of the RHH under the same relative density. In the other words, the new honeycombs show higher specific compressive stiffness and shear stiffness than the RHH. This result indicates the new designs coincide with the standard of high specific stiffness.

As summarized by Grenestedt [46], the scaling of effective Young's modulus (E^*) of 2D cellular structures with relative density is:

$$\frac{E^*}{E_0} = C\left(\Delta\rho\right)^m \tag{43}$$

where $m = 1$ for stretching controlled micro structures; $m = 3$ for bending controlled micro structures. Using Eq.(43) to fit the data plotted in Fig.13, we can attain the corresponding coefficients C and m for each case. It was found from Fig.13 (a) and (b) that, both the *x*- and *y*- directional Young's modulus of the RHH scale approximately cubically with relative density ($m = 2.973$ for *x* direction while $m = 2.961$ for *y* direction). This indicates that the RHH is the pure bending dominated structure. Under the same relative density, the Young's modulus of the new honeycombs in both *x* and *y* directions increase with R/l_1. For the new honeycombs with $R/l_1 = 2$, $m = 2.770$ for *x* direction while $m = 2.620$ for *y* direction. Apparently, the exponent m for the new honeycombs with $R/l_1 = 2$ is close to 3 which reveals the new honeycombs with $R/l_1 = 2$ are also a bending dominated structure. In the case of $R/l_1 = 4$, m dramatically deviates from 3 ($m = 2.356$ for *x*

direction while $m=2.097$ for *y* direction), which shows that the axial deformation of the microstructure becomes significant gradually with R/l_1 increasing. As R/l_1 rises to 10, the exponent m clearly titled toward to 1 ($m=1.629$ for *x* direction while $m=1.438$ for *y* direction). Finally, an approximate linear relation between the Young's modulus and relative density was observed in the case when $R/l_1=20$. In summary, the exponent m tends to deviate from 3 and approach to 1 with R/l_1 increasing. According to the result by Grenestedt [46], the dominated deformation mode of new structures transforms from bending to stretching as R/l_1 varies from 2 to 20. Given above, the dominated deformation mode of the new honeycomb is flexible and a special dominated deformation mode between pure bending and stretching can be achieved with some certain values of R/l_1.

Fig.13(c) illustrates the variation of the in-plane shear modulus with the relative density. Using a similar power function form as Eq.(43), i.e., $\left(G_{xy}/E_0\right)=D\left(\Delta\rho\right)^n$, fitting curve for each case was plotted in Fig.13(c). It is found that, the shear modulus increases with R/l_1 under the same relative density. And, the Type II honeycomb shows higher shear modulus than Type I. An approximate cubic growth relation between the relative density and shear modulus was observed in both the RHH and the new honeycombs with low R/l_1 ($R/l_1=2$, $R/l_1=4$). With R/l_1 increasing, the exponent n tends to deviate from 3 and approach to 1. In view of this, the relation between the relative density and shear modulus can also be considered as a criterion for identifying the dominated deformation mode of cellular structures.

4. Conclusions

In this paper, two types of new honeycombs with curved inserts were developed based on the most common auxteic honeycomb, RHH. The slope-deflection equations for both the straight and curved wall were established with fully considering the bending, shearing and stretching deformations. By combing the slope-deflection

equations of all the walls in the unit cell (or representative block) we determined, the theoretical models for the in-plane Young's modulus, Poisson's ratio and shear modulus of the new honeycombs were developed. FE models with 3D solid element (Solid 186) were built to verify the developed theoretical models and a good agreement between the FE simulations and theoretical predictions was observed.

Both the theoretical and FE results show that the two new types of honeycombs display equality in Young's modulus and Poisson's ratio, while the shear modulus of the Type II new honeycomb is slightly higher than that of the Type I. Influences of the micro geometric parameters on the macroscopic mechanical properties were fully discussed. A desired stiffness and auxeticity can be achieved by tailoring the micro geometric parameters. For example, we can achieve a minimum value of E_x^{I}/E_0 (or E_x^{II}/E_0) at around $\theta_0 = 25°$ and a maximum negative value of ν_{yx}^{I} (or ν_{yx}^{II}) at around $\theta_0 = 40°$; Increasing the ratio of t_0/l_0 can result in a high Young's modulus and shear modulus but a weak auxeticity; Increasing the ratio of R/l_1, the dominated deformation mode of the structures gradually varies from bending to stretching. This is the root cause for the phenomenon that the Young's modulus and shear modulus of the new honeycombs increase with R/l_1. It is noted that the new honeycombs show a flexible dominated deformation mode and a special dominated deformation mode intermediate between pure bending and stretching can be achieved.

In summary, the two new honeycombs we developed meet the design standards of high specific stiffness. The work would provide a good guideline for the development of the auxetic structures with improved mechanical properties and design flexibility. It should be noted that, full experimental investigations will be presented in our next paper.

Acknowledgments

The authors would like to thank the funding support from the Research Grants Council of Hong Kong Special Administrative Region Government for the

NSFC/RGC Joint Research Scheme (Grant number: N_PolyU516/20), the National Natural Science Foundation of China (Grant numbers: 11672338) and the Fundamental Research Funds for the Central Universities (Grant No. 11621015).

Conflict of interest statement

The authors declare that they have no conflict of interest

Appendix A. In-plane shear modulus of the Type II honeycomb (G_{xy}^{II})

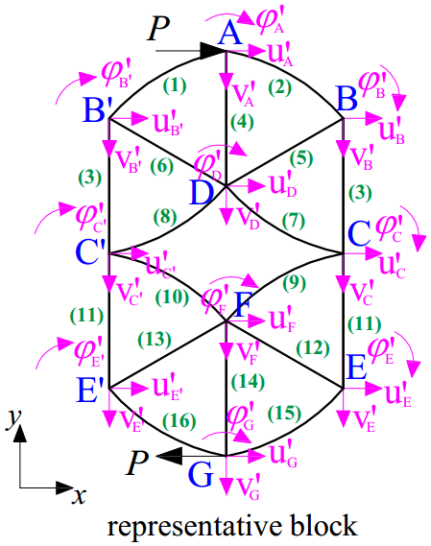

Fig.A.1. Free body of diagram of the representative block of the Type II new honeycomb.

In this appendix, we presented a theoretical model for the in-plane shear modulus of the Type II honeycomb (G_{xy}^{II}). Similar to the derivation in Section 3.1.2, the force-displacement equation for each wall in Fig.A.1 can be attained by using Eqs.(34) and (36). According to the forces balances at points A, B, C, D, E , F and G, a relation between the forces and the displacements over the whole representative block was given:

$$\mathbf{F}_{(21\times1)}^{\mathbf{II}} = \mathbf{Z}_{(21\times21)}^{\mathbf{II}}\mathbf{D}_{(21\times1)}^{\mathbf{II}} \tag{A.1}$$

with

$$\mathbf{D}_{(21\times1)}^{\mathbf{II}} = \left(u_A, v_A, \varphi_A, u_B, v_B, \varphi_B, u_C, v_C, \varphi_C, u_D, v_D, \varphi_D, u_E, v_E, \varphi_E, u_F, v_F, \varphi_F, u_G, v_G, \varphi_G\right)^T$$

$$\mathbf{F}^{\mathbf{II}}_{(\mathbf{21\times1})}=\left(F_{Ax},F_{Ay},M_{A},F_{Bx},F_{By},M_{B},F_{Cx},F_{Cy},M_{C},F_{Dx},F_{Dy},M_{D},F_{Ex},F_{Ey},M_{E},F_{Fx},F_{Fy},M_{F},F_{Gx},F_{Gy},M_{G}\right)^{T}$$

$$=\left(\frac{P}{E_0},0,0,0,0,0,0,0,0,0,0,0,0,0,0,0,0,0,\frac{-P}{E_0},0,0\right)^{T}$$

$$\mathbf{Z}^{\mathbf{II}}_{(21\times21)}=\begin{pmatrix}
\delta_{II}^{(1)}G_{22}^{(1)}\lambda_{II}^{(1)}+\delta_{II}^{(2)}G_{11}^{(2)}\lambda_{II}^{(2)}+\delta_{II}^{(4)}K_{11}^{(4)}\lambda_{II}^{(4)} & \delta_{II}^{(1)}G_{21}^{(1)}\lambda_{II}^{(1)}+\delta_{II}^{(2)}G_{12}^{(2)}\lambda_{II}^{(2)} & 0 & \delta_{II}^{(4)}K_{12}^{(4)}\lambda_{II}^{(4)} & 0 & 0 & 0\\
\delta_{II}^{(1)}G_{12}^{(1)}\lambda_{II}^{(1)}+\delta_{II}^{(2)}G_{21}^{(2)}\lambda_{II}^{(2)} & \delta_{II}^{(1)}G_{11}^{(1)}\lambda_{II}^{(1)}+\delta_{II}^{(2)}G_{22}^{(2)}\lambda_{II}^{(2)}+\delta_{II}^{(3)}K_{11}^{(3)}\lambda_{1}^{(3)}+\delta_{II}^{(5)}K_{11}^{(5)}\lambda_{II}^{(5)}+\delta_{II}^{(6)}K_{11}^{(6)}\lambda_{II}^{(6)} & \delta_{II}^{(3)}K_{12}^{(3)}\lambda_{II}^{(3)} & \delta_{II}^{(5)}K_{12}^{(5)}\lambda_{II}^{(5)}+\delta_{II}^{(6)}K_{12}^{(6)}\lambda_{II}^{(6)} & 0 & 0 & 0\\
0 & \delta_{II}^{(3)}K_{21}^{(3)}\lambda_{II}^{(3)} & \delta_{II}^{(3)}K_{22}^{(3)}\lambda_{II}^{(3)}+\delta_{II}^{(7)}G_{11}^{(7)}\lambda_{II}^{(7)}+\delta_{II}^{(8)}G_{22}^{(8)}\lambda_{II}^{(8)}+\delta_{II}^{(9)}G_{22}^{(9)}\lambda_{II}^{(9)}+\delta_{II}^{(10)}G_{11}^{(10)}\lambda_{II}^{(10)}+\delta_{II}^{(11)}K_{11}^{(11)}\lambda_{II}^{(11)} & \delta_{II}^{(7)}G_{12}^{(7)}\lambda_{II}^{(7)}+\delta_{II}^{(8)}G_{21}^{(8)}\lambda_{II}^{(8)} & \delta_{II}^{(11)}K_{12}^{(11)}\lambda_{II}^{(11)} & \delta_{II}^{(9)}G_{21}^{(9)}\lambda_{II}^{(9)}+\delta_{II}^{(10)}G_{12}^{(10)}\lambda_{II}^{(10)} & 0\\
\delta_{II}^{(4)}K_{21}^{(4)}\lambda_{II}^{(4)} & \delta_{II}^{(5)}K_{21}^{(5)}\lambda_{II}^{(5)}+\delta_{II}^{(6)}K_{21}^{(6)}\lambda_{II}^{(6)} & \delta_{II}^{(7)}G_{21}^{(7)}\lambda_{II}^{(7)}+\delta_{II}^{(8)}G_{12}^{(8)}\lambda_{II}^{(8)} & \delta_{II}^{(4)}K_{22}^{(4)}\lambda_{II}^{(4)}+\delta_{II}^{(5)}K_{22}^{(5)}\lambda_{II}^{(5)}+\delta_{II}^{(6)}K_{22}^{(6)}\lambda_{II}^{(6)}+\delta_{II}^{(7)}G_{22}^{(7)}\lambda_{II}^{(7)}+\delta_{II}^{(8)}G_{11}^{(8)}\lambda_{II}^{(8)} & 0 & 0 & 0\\
0 & 0 & \delta_{II}^{(11)}K_{21}^{(11)}\lambda_{II}^{(11)} & 0 & \delta_{II}^{(11)}K_{22}^{(11)}\lambda_{II}^{(11)}+\delta_{II}^{(12)}K_{22}^{(12)}\lambda_{II}^{(12)}+\delta_{II}^{(13)}K_{22}^{(13)}\lambda_{II}^{(13)}+\delta_{II}^{(15)}G_{11}^{(15)}\lambda_{II}^{(15)}+\delta_{II}^{(16)}G_{22}^{(16)}\lambda_{II}^{(16)} & \delta_{II}^{(12)}K_{21}^{(12)}\lambda_{II}^{(12)}+\delta_{II}^{(13)}K_{21}^{(13)}\lambda_{II}^{(13)} & \delta_{II}^{(15)}G_{12}^{(15)}\lambda_{II}^{(15)}+\delta_{II}^{(16)}G_{21}^{(16)}\lambda_{II}^{(16)}\\
0 & 0 & \delta_{II}^{(9)}G_{12}^{(9)}\lambda_{II}^{(9)}+\delta_{II}^{(10)}G_{21}^{(10)}\lambda_{II}^{(10)} & 0 & \delta_{II}^{(12)}K_{12}^{(12)}\lambda_{II}^{(12)}+\delta_{II}^{(13)}K_{12}^{(13)}\lambda_{II}^{(13)} & \delta_{II}^{(9)}G_{11}^{(9)}\lambda_{II}^{(9)}+\delta_{II}^{(10)}G_{22}^{(10)}\lambda_{II}^{(10)}+\delta_{II}^{(12)}K_{11}^{(12)}\lambda_{II}^{(12)}+\delta_{II}^{(13)}K_{11}^{(13)}\lambda_{II}^{(13)}+\delta_{II}^{(14)}K_{11}^{(14)}\lambda_{II}^{(14)} & \delta_{II}^{(14)}K_{12}^{(14)}\lambda_{II}^{(14)}\\
0 & 0 & 0 & 0 & \delta_{II}^{(15)}G_{21}^{(15)}\lambda_{II}^{(15)}+\delta_{II}^{(16)}G_{12}^{(16)}\lambda_{II}^{(16)} & \delta_{II}^{(14)}K_{21}^{(14)}\lambda_{II}^{(14)} & \delta_{II}^{(14)}K_{22}^{(14)}\lambda_{II}^{(14)}+\delta_{II}^{(15)}G_{22}^{(15)}\lambda_{II}^{(15)}+\delta_{II}^{(16)}G_{11}^{(16)}\lambda_{II}^{(16)}
\end{pmatrix}$$

$$\boldsymbol{\lambda}_{\mathbf{II}}^{(1)}=\boldsymbol{\lambda}_{\mathbf{II}}^{(9)}=\begin{pmatrix}\cos\theta_1 & -\sin\theta_1 & 0\\ -\sin\theta_1 & -\cos\theta_1 & 0\\ 0 & 0 & 1\end{pmatrix},\boldsymbol{\delta}_{\mathbf{II}}^{(1)}=\boldsymbol{\delta}_{\mathbf{II}}^{(9)}=\left(\boldsymbol{\lambda}_{\mathbf{II}}^{(1)}\right)^{-1}=\begin{pmatrix}\cos\theta_1 & -\sin\theta_1 & 0\\ -\sin\theta_1 & -\cos\theta_1 & 0\\ 0 & 0 & 1\end{pmatrix};$$

$$\boldsymbol{\lambda}_{\mathbf{II}}^{(2)}=\boldsymbol{\lambda}_{\mathbf{II}}^{(10)}=\begin{pmatrix}\cos\theta_1 & \sin\theta_1 & 0\\ \sin\theta_1 & -\cos\theta_1 & 0\\ 0 & 0 & 1\end{pmatrix},\boldsymbol{\delta}_{\mathbf{II}}^{(2)}=\boldsymbol{\delta}_{\mathbf{II}}^{(10)}=\left(\boldsymbol{\lambda}_{\mathbf{II}}^{(2)}\right)^{-1}=\begin{pmatrix}\cos\theta_1 & \sin\theta_1 & 0\\ \sin\theta_1 & -\cos\theta_1 & 0\\ 0 & 0 & 1\end{pmatrix};$$

$$\boldsymbol{\lambda}_{\mathbf{II}}^{(3)}=\boldsymbol{\lambda}_{\mathbf{II}}^{(4)}=\boldsymbol{\lambda}_{\mathbf{II}}^{(11)}=\boldsymbol{\lambda}_{\mathbf{II}}^{(14)}=\begin{pmatrix}0 & 1 & 0\\ 1 & 0 & 0\\ 0 & 0 & 1\end{pmatrix},\boldsymbol{\delta}_{\mathbf{II}}^{(3)}=\boldsymbol{\delta}_{\mathbf{II}}^{(4)}=\boldsymbol{\delta}_{\mathbf{II}}^{(11)}=\boldsymbol{\delta}_{\mathbf{II}}^{(14)}=\left(\boldsymbol{\lambda}_{\mathbf{II}}^{(3)}\right)^{-1}=\begin{pmatrix}0 & 1 & 0\\ 1 & 0 & 0\\ 0 & 0 & 1\end{pmatrix};$$

$$\boldsymbol{\lambda}_{\mathbf{II}}^{(5)}=\boldsymbol{\lambda}_{\mathbf{II}}^{(13)}=\begin{pmatrix}-\cos\theta_0 & \sin\theta_0 & 0\\ \sin\theta_0 & \cos\theta_0 & 0\\ 0 & 0 & 1\end{pmatrix},\boldsymbol{\delta}_{\mathbf{II}}^{(5)}=\boldsymbol{\delta}_{\mathbf{II}}^{(13)}=\left(\boldsymbol{\lambda}_{\mathbf{II}}^{(5)}\right)^{-1}=\begin{pmatrix}-\cos\theta_0 & \sin\theta_0 & 0\\ \sin\theta_0 & \cos\theta_0 & 0\\ 0 & 0 & 1\end{pmatrix};$$

$$\boldsymbol{\lambda}_{\mathbf{II}}^{(6)}=\boldsymbol{\lambda}_{\mathbf{II}}^{(12)}=\begin{pmatrix}\cos\theta_0 & \sin\theta_0 & 0\\ \sin\theta_0 & -\cos\theta_0 & 0\\ 0 & 0 & 1\end{pmatrix},\boldsymbol{\delta}_{\mathbf{II}}^{(6)}=\boldsymbol{\delta}_{\mathbf{II}}^{(12)}=\left(\boldsymbol{\lambda}_{\mathbf{II}}^{(6)}\right)^{-1}=\begin{pmatrix}\cos\theta_0 & \sin\theta_0 & 0\\ \sin\theta_0 & -\cos\theta_0 & 0\\ 0 & 0 & 1\end{pmatrix};$$

$$\boldsymbol{\lambda}_{\mathbf{II}}^{(7)}=\boldsymbol{\lambda}_{\mathbf{II}}^{(16)}=\begin{pmatrix}-\cos\theta_1 & -\sin\theta_1 & 0\\ -\sin\theta_1 & \cos\theta_1 & 0\\ 0 & 0 & 1\end{pmatrix},\boldsymbol{\delta}_{\mathbf{II}}^{(7)}=\boldsymbol{\delta}_{\mathbf{II}}^{(16)}=\left(\boldsymbol{\lambda}_{\mathbf{II}}^{(7)}\right)^{-1}=\begin{pmatrix}-\cos\theta_1 & -\sin\theta_1 & 0\\ -\sin\theta_1 & \cos\theta_1 & 0\\ 0 & 0 & 1\end{pmatrix};$$

$$\boldsymbol{\lambda}_{\mathbf{II}}^{(8)}=\boldsymbol{\lambda}_{\mathbf{II}}^{(15)}=\begin{pmatrix}-\cos\theta_1 & \sin\theta_1 & 0\\ \sin\theta_1 & \cos\theta_1 & 0\\ 0 & 0 & 1\end{pmatrix},\boldsymbol{\delta}_{\mathbf{II}}^{(8)}=\boldsymbol{\delta}_{\mathbf{II}}^{(15)}=\left(\boldsymbol{\lambda}_{\mathbf{II}}^{(8)}\right)^{-1}=\begin{pmatrix}-\cos\theta_1 & \sin\theta_1 & 0\\ \sin\theta_1 & \cos\theta_1 & 0\\ 0 & 0 & 1\end{pmatrix}.$$

Similar to the details introduced in Section 3.1.2, $\mathbf{K}_{\mathbf{mn}}^{(\mathbf{k})}$ and $\mathbf{G}_{\mathbf{mn}}^{(\mathbf{k})}$ $(\mathbf{m}=1,2;\mathbf{n}=1,2)$ in the matrix $\mathbf{Z}_{(21\times21)}^{\mathbf{II}}$, the component of the stiffness matrix of the cell wall $\mathbf{k}$ in Fig.A.1, can be attained from Eq. (34) and Eq.(36), respectively. $\boldsymbol{\delta}_{\mathbf{II}}^{\mathbf{k}}$ is the coordinate transformation matrix from the local coordinate to the global coordinate (the Cartesian coordinates of x-y in Fig.A.1), while $\boldsymbol{\lambda}_{\mathbf{II}}^{\mathbf{k}}$ denotes the coordinate transformation matrix from the global coordinate to the local coordinate.

From Eq.(A.1), the displacements of all the points can be expressed as a known function of the shear force, P. The shear stress and strain is:

$$\tau_{xy}^{\mathrm{II}}=\frac{P}{2Hl_0\cos\theta_0}\quad , \tag{A.2}$$

and

$$\gamma_{xy}^{\mathrm{II}}=\frac{\mathrm{u_A}-\mathrm{u_G}}{2\left(h_0-l_0\sin\theta_0\right)}\quad , \tag{A.3}$$

respectively. Finally the in-plane shear modulus for the Type II honeycomb is calculated by $G_{xy}^{\mathrm{II}}=\tau_{xy}^{\mathrm{II}}/\gamma_{xy}^{\mathrm{II}}$.

References

[1] Gibson L J, Ashby M F. Cellular Solids: Structure and Properties, second edit. Cambridge University Press, New York, 1997.

[2] Zhang Q, Yang X, Li P, Huang G, Feng S, Shen C, Han B, Zhang X, Jin F, Xu F, Lu T J. Bioinspired engineering of honeycomb structure-Using nature to inspire human innovation. Progress in Materials Science 2015; 74: 332-400.

[3] Zadpoor A A. Mechanical meta-materials. Materials Horizons 2016; 3: 371-381.

[4] Masters I G, Evans K E. Models for the elastic deformation of honeycombs. Composite Structures 1996; 35(4): 403-422.

[5] Zhu H X, Mills N J. The in-plane non-linear compression of regular honeycombs. International Journal of Solids and Structures 2000; 37(13): 1931-1949.

[6] Zhu H X, Chen C Y. Combined effects of relative density and material distribution on the mechanical properties of metallic honeycombs. Mechanics of Materials 2011; 43: 276-286.

[7] Hu L L, Yu T X. Mechanical behavior of hexagonal honeycombs under low-velocity impact-theory and simulations. International Journal of Solids and Structures 2013; 50(20-21): 3152-3165.

[8] Malek S, Gibson L, Effective elastic properties of periodic hexagonal honeycombs. Mechanics of Materials 2015; 91: 226-240.

[9] Lakes R. Foam structures with a negative Poisson's ratio. Science 1987; 235(4792): 1038-1040.

[10] Evans K E, Nkansah M A, Hutchinson I J, Rogers S C. Molecular network design Nature 1991; 353(6340): 124-124.

[11] Evans K E, Alderson A. Auxetic materials: functional materials and structures from lateral thinking! 2000; 12(9): 617-628.

[12] Lim T C. Auxetic Materials and Structures. Springer, Singapore, 2015.

[13] Hu H, Zhang M, Liu Y. Auxetic Textiles, Elsevier, 2019.

[14] Salit V, Weller T, On the feasibility of introducing auxetic behavior into thin-walled structures. Acta Materialia 2009; 57: 125-135.

[15] Prawoto Y. Seeing auxetic materials from the mechanics point of view: A structural review on the negative Poisson's ratio. Computational Materials Science 2012; 58:140-153.

[16] Zhang W, Ma Z, Hu P. Mechanical properties of a cellular vehicle body structure with negative Poisson's ratio and enhanced strength. Journal of Reinforced Plastics and Composites 2014; 33(4): 342-349.

[17] Ma Y, Scarpa F, Zhang D, Zhu B, Chen L, Hong J. A nonlinear auxetic structural vibration damper with metal rubber particles. Smart Materials and Structures 2013; 22(8): 084012.

[18] Jiang Y, Liu Z, Matsuhisa N, Qi D, Leow W R, Yang H, Yu J, Chen G, Liu Y,

Wan C, Liu Z, Chen X. Auxetic Mechanical Metamaterials to Enhance Sensitivity of Stretchable Strain Sensors. Advanced Materials 2018; 30(12): 1706589.

[19] Ferguson W J G, Kuang Y, Evans K E, Smith C W, Zhu M. Auxetic structure for increased power output of strain vibration energy harvester. Sensors and Actuators A 2018; 282: 90-96.

[20] Zahra T, Dhanasekar M. Characterisation of cementitious polymer mortar-Auxetic foam composites. Construction and Building Materials 2017; 147: 143-159.

[21] Duncan O, Shepherd T, Moroney C, Foster L, Venkatraman P D, Winwood K, Allen T, Alderson A. Review of Auxetic Materials for Sports Applications: Expanding Options in Comfort and Protection. 2018; 8: 941, doi:10.3390/app8060941.

[22] Bezazi A, Scarpa F, Remillat C. A novel centresymmetric honeycomb composite structure. Composite Structures 2005; 71: 356-364.

[23] Meena K, Singamneni S. A new auxetic structure with significantly reduced stress concentration effects. Materials and Design 2019; 173: 107779.

[24] Qi C, Jiang F, Remennikov A, Pei L Z, Liu J, Wang J S, Liao X W, Yang S. Quasi-static crushing behavior of novel re-entrant circular auxetic honeycombs. Composites Part B: Engineering 2020; 197: 108117.

[25] Lu Z X, Li X, Yang Z Y, Xie F. Novel structure with negative Poisson's ratio and enhanced Young's modulus. Composite Structures 2016; 138: 243-252.

[26] Fu M H, Chen Y, Hu L L. A novel auxetic honeycomb with enhanced in-plane stiffness and buckling strength. Composite Structures 2017; 160, 574-585.

[27] Fu M H, Chen Y, Hu L L. Bilinear elastic characteristic of enhanced auxetic honeycombs. Composite Structures 2017; 175: 101-110.

[28] Tatlıer M S, Öztürk M, Baran T. Linear and non-linear in-plane behaviour of a modified re-entrant core cell. Engineering Structures 2021; 234: 111984.

[29] Rayneau-Kirkhope D. Stiff auxetics: Hierarchy as a route to stiff, strong lattice based auxetic meta-materials. Scientific Reports 2018; 8: 12437.

[30] Gao Y, Zhou Z, Hu H, Xiong J. New concept of carbon fiber reinforced composite 3D auxetic lattice structures based on stretching-dominated cells.

Mechanics of Materials 2021; 152: 103661.

[31] Gao Y, Wu Q, Wei X, Zhou Z, Xiong J. Composite tree-like re-entrant structure with high stiffness and controllable elastic anisotropy. International Journal of Solids and Structures 2020; 206:170-182.

[32] Yang L, Harrysson O, West H, Cormier D. Modeling of uniaxial compression in a 3D periodic re-entrant lattice structure. Journal of Materials Science 2013; 48: 1413-1422.

[33] Wang X T, Wang B, Li X W, Ma L. Mechanical properties of 3D re-entrant auxetic cellular structures, International Journal of Mechanical Sciences 2020; 131-132: 396-407.

[34] Fu M, Chen Y, Zhang W, Zheng B. Experimental and numerical analysis of a novel three-dimensional auxetic metamaterial. Phys. Status Solidi B 2016; 253(8): 1565-1575.

[35] Simone A E, Gibson L J. Aluminum foams produced by liquid-state processes. Acta Materialia 1998; 46(9): 3109-3123.

[36] Simone A E, Gibson L J. Effects of solid distribution on the stiffness and strength of metallic foams. Acta Materialia 1998; 46(6): 2139-2150.

[37] Grenestedt J L. Influence of wavy imperfections in cell walls on elastic stiffness of cellular solids. Journal of the Mechanics and Physics of Solids 1998; 46(1): 29-50.

[38] Chen C, Lu T J, Fleck N A. Effect of imperfections on the yielding of two-dimensional foams. Journal of the Mechanics and Physics of Solids 1999; 47(11): 2235-2272.

[39] Huang J S, Chang F M. Effects of curved cell edges on the stiffness and strength of two-dimensional cellular solids. Composite Structures 2005; 69(2):183-191.

[40] Li K, Gao X L, Subhash G. Effects of cell shape and cell wall thickness variations on the elastic properties of two-dimensional cellular solids. International Journal of Solids and Structures 2005; 42:1777-1795.

[41] Lin T C. Yang M Y, Huang J S. Effects of solid distribution on the out-of-plane elastic properties of hexagonal honeycombs. Composite Structures 2013; 100(5): 436-442.

[42] Harkati A, Harkati E H, Bezazi A, Scarpa F, Ouisse M. Out-of-plane elastic constants of curved cell walls honeycombs. Composite Structures 2021; 268: 113959.

[43] Ingrole A, Hao A, Liang R. Design and modeling of auxetic and hybrid honeycomb structures for in-plane property enhancement. Materials & Design 2017; 117, 72-83.

[44] Harkati A, Boutagouga D, Harkati E, Bezazi A, Scarpa F, Ouisse M. In-plane elastic constants of a new curved cell walls honeycomb concept. Thin-Walled Structures 2020; 149: 106613.

[45] Ma X L, Zhang G T, Xiao Z H. The slope-displacement equation used for the circular curved bar of a uniform cross section. Journal of Xinjiang Institute of Technology 1999; 20(2): 79-83. (in chinese)

[46] Grenestedt J L. Effective elastic behavior of some models for perfect cellular solids. International Journal of Solids and Structures 1999; 36(10):1471-1501.